# Simulated Moon agglutinates obtained from zeolite precursor by means of a low-cost and scalable synthesis method

Francesca Stefania Freyria, Antonello Marocco, Serena Esposito, Barbara Bonelli, Gabriele Barrera, Paola Tiberto, Paolo Allia, Pauline Oudayer, Aurélien Roggero, Jean-Charles Matéo-Vélez, et al.

ACS EARTH AND SPACE CHEMISTRY

Article

# Simulated Moon agglutinates obtained from zeolite precursor by means of a low-cost and scalable synthesis method

Francesca Stefania Freyria, Antonello Marocco, Serena ESPOSITO, Barbara Bonelli, Gabriele Barrera, Paola Tiberto, Paolo Allia, Pauline Oudayer, Aurélien Roggero, Jean-Charles Matéo-Vélez, Eric Dantras, and Michele Pansini

*ACS Earth Space Chem.*, **Just Accepted Manuscript** • DOI: 10.1021/acsearthspacechem.9b00042 • Publication Date (Web): 04 Jun 2019

# Simulated Moon agglutinates obtained from zeolite precursor by means of a low-cost and scalable synthesis method

Francesca S. Freyria[1], Antonello Marocco[2], Serena Esposito[1,*], Barbara Bonelli[1*], Gabriele Barrera[3], Paola Tiberto[3], Paolo Allia,[1,3] Pauline Oudayer[4], Aurélien Roggero[5], Jean-Charles Matéo-Vélez[4], Eric Dantras[6], Michele Pansini[2]

[1]Department of Applied Science and Technology and INSTM Unit of Torino – Politecnico, Politecnico di Torino, Corso Duca degli Abruzzi 24, 10129, Torino, Italy.

[2]Department of Civil and Mechanical Engineering and INSTM Research Unit, Università degli Studi di Cassino e del Lazio Meridionale, Via G. Di Biasio 43, Cassino, FR 03043, Italy

[3]INRiM Torino, Advanced Materials for Metrology and Life Sciences, Strada delle Cacce 91, 10143 Torino, Italy

[4]ONERA, The French Aerospace Lab, 2 Avenue Edouard Belin, Toulouse, France

[5]CIRIMAT-ENSIACET, INP-ENSIACET, 4 allée Emile Monso, Toulouse, France

[6]CIRIMAT-Physique des Polymères, Université Toulouse 3 - Paul Sabatier, 118 route de Narbonne, Toulouse, France

**Keywords:** *nanocomposites; agglutinates; lunar soil; nanophase iron; magnetic properties; electric properties.*

Corresponding Authors: Serena Esposito *(serena_esposito@polito.it); Barbara Bonelli (barbara.bonelli@polito.it)*

## Abstract

A practical, inexpensive and scalable synthesis method, based on the $Fe^{2+}$ exchange of two commercial zeolites (*i.e.* Na-A and Na-X) followed by reductive thermal treatment at 1023 K, allowed obtaining nanocomposites where $Fe^0$ nanoparticles are dispersed within an agglutinitic glassy matrix stemming from the amorphization of the zeolite precursor.

The materials were characterized by means of atomic absorption spectrometry; X-ray powder diffraction followed by Rietveld analysis; transmission electron microscopy; $N_2$ adsorption/desorption isotherms at 77 K; measurements of grain size distribution; magnetic properties measurements; broadband dielectric spectroscopy and DC conductivity measurements.

The physico-chemical characterization showed that the final nanocomposites could be suitable as a new type of “simulated” Moon agglutinate, a component that is lacking in most of the current lunar regolith/soil simulants.

## Introduction

Although NASA seems keener on Mars missions, future manned space missions to the Moon have been already planned (*e.g.* by the China National Space Administration and the European Space Agency), with the aim of using it as a test bed either for missions to Mars (and other airless planetary bodies) or for field-applications of remote sensing instrumentation.[1,2 3]

The Moon is the closest planetary body to Earth without atmosphere, where geological soil has been directly sampled. As that of other planetary bodies, its surface is covered by "regolith", a complex, pulverized target material (with no equivalent on Earth) that is the result of continuous space weathering processes. The latter are mainly comminution, followed by cementation and chemical modification by means of (micro)meteorites bombardment, solar wind, irradiation and sputtering of cosmic and galactic rays.[1]

From a practical point of view, a thorough knowledge of the physico-chemical properties of the lunar regolith is crucial, as it can interact with electronic devices, for instance, and be dangerous for human health. Moreover, it would be very important to assess the possibility of *in situ* resource utilization (ISRU), *i.e.* to exploit the regolith for water and oxygen extraction, energy production, habitat construction, *etc*.[4]

The thickness of the lunar regolith varies from average 4-5 m in *maria* to 10-20 m in older highland regions.[4,5,6] Its components are mineral fragments with nm-mm grain size; larger lithic fragments; glass spheres and shards; solar ray- and galactic ray-implanted molecules, atoms and sub-atomic particles; agglutinates and nanophase iron (np-$Fe^0$).[4,7] With respect to component sizes, in 1991, McKay *et al.* defined "lunar regolith" as the ensemble of components with < 1 cm size deriving from disaggregation phenomena, and should basically coincide with the so-called "lunar soil".[8] Since 2006, the term "lunar soil" has been instead applied only to the < 1mm fraction.[7,9] The components size is important: former Apollo missions reported some

toxic effects, like dermal irritation, penetration and ocular damages, as well as pulmonary and cardiovascular diseases,[5] because the finest part of lunar soil (*i.e.* those components with an aerodynamic diameter < 10 μm) can damage the human respiratory system. Particularly, the fraction with 2.5-10 μm diameter can deposit within trachea and bronchiole ducts; the fine fraction (0.1-2.5 μm) can penetrate the respiratory zone, and the ultra-fine fraction (less than 0.1 μm) can interact with mucous membranes or be trapped by macrophages.[10,11]

The absence of atmosphere, the solar wind and the continuous chemical reduction can confer electrostatic charge to the lunar soil and create three main fractions, namely levitated dust (< 10 μm at altitudes of 10–30 cm), ejecta and meteoroids.[3,12] Besides being harmful to humans, the various fractions may interact with surfaces both electrostatically and mechanically (owing to its degree of abrasiveness, penetration and friction ability).[2,13] Moreover, in airless environment, under constant UV radiation and regular and hypervelocity bombardment by meteorites and micrometeorites, small fractions of the lunar regolith may melt, and their surface may become highly reactive: the molten phase quenches to a glass that welds the mineral and lithic particles into aggregate grains, giving rise to the aforementioned "agglutinates",[14] characterized by the size of few nm to several μm, and containing plenty of Fe particles.[1,15,16] The latter occur either as larger "globules" (average size of 120 ± 20 nm)[17] or as smaller metallic iron nanoparticles, *i.e.* np-$Fe^0$ with dimensions in the 3-33 nm range and average size of 7 nm.[18] At variance with terrestrial minerals, in lunar agglutinates iron cannot occur as $Fe^{3+}$ species, but only as $Fe^0$ and/or $Fe^{2+}$ species,[14] which may produce reactive oxygen species dangerous to human cells.[19,20] Consequently, agglutinates can dissolve into body fluids, giving rise to dangerous Fenton's reaction,[10,11,21] and can be harmful to astronauts, whereas the abrasive and magnetic properties may be harmful to spacecraft devices.

Notwithstanding the need of studying in detail the lunar regolith properties, the scarcity of the actual Moon soil has resulted in the creation of several lunar regolith/soil simulants,[22] some of them being listed in Table 1. Since the first simulant, named JSC-1, standardized by NASA in 1994,[5] many simulants have been produced and studied. At the end of 2010, the LEAG-CAPTEM simulant working group wrote an exhaustive report about the state of art of the simulants and their utilization.[23] Afterwards, new simulants (*e.g.* CLDS-i and BHLD20)[21,22] have been developed, to better figure out all the possible drawbacks that lunar regolith/soil can cause.

As shown in Table 1, the available simulants often lack the agglutinates fraction, likely because it is the most difficult to reproduce. An efficient (but expensive and scarcely scalable) method to synthesize agglutinitic glasses is based on a sol-gel synthesis, starting from silica organosilanes (*e.g.* TEOS) or pre-condensed silica commercial solutions, used as precursors of the glassy matrix, and nitrates, used as precursors of oxides and np-$Fe^0$: the so-produced agglutinates were sometimes added to the JSC-1Af simulant (Table 1).[12] In 2010, Spray proposed instead the use of a friction welding apparatus for the production of a lunar regolith agglutinate simulant (lacking the np-$Fe^0$ component) and suitable for lunar engineering applications: the author mentioned that the inclusion of np-$Fe^0$ would have been a further improvement, facilitating the ISRU extraction technologies and making the agglutinate simulant more realistic from the point of view of electrostatic properties.[4]

To the best of our knowledge, only the CLDS-i simulant already contains agglutinates with embedded metallic iron (obtained from basalts and metallic iron targets bombarded at low pressure in nitrogen environment)[21] and according to the literature, the production of a reliable and inexpensive simulant is still far for being fulfilled.[22] Here, we report the synthesis and characterization of simulated Moon agglutinates containing embedded np-$Fe^0$ and having

physico-chemical features comparable to the actual agglutinates, by means of a smart process[24,25] for the production magnetic nanocomposites. The process envisages two steps, *i.e.* a heavy metal (Fe, Ni, or Co) cations exchange of a commercial zeolite and a thermal treatment at relatively mild temperatures (773-1123 K range) under reducing atmosphere (2.0 vol.% $H_2$ in Ar).[26–30] The nanocomposites were already successfully used for other biochemical and environmental applications.[31,32] In this work, two np-$Fe^0$ rich nanocomposites, obtained from two commercial zeolites (Na-A and Na-X), were characterized by means of physico-chemical, structural, magnetic and electric techniques, in order assess whether they have the proper features to be considered as simulants of the lunar regolith agglutinates.

**Table 1**: List of the most common and/or recently developed lunar regolith/soil simulants. Those simulants developed only for geotechnical or optical purposes (having mineral and/or chemical composition) are not reported here. Other, more exhaustive, lists can be found in refs [23,33]

| Simulant name | Country | Presence of Agglutinates with np-$Fe^0$ | Modification | Purpose | Ref | Year* |
|---|---|---|---|---|---|---|
| JSC-1/1A/1AF/1AC/2A Johnson Space Center | USA | No | np-$Fe^0$ embedded in a glassy matrix by sol-gel synthesis, followed by reduction at high temperature[16] | General | [23,34,35] | 1994 |
| LHS-1 Lunar Highlands Simulant | USA | No | | General | [33] | Since 2014 |
| LMS-1 Lunar Mare Simulant | USA | No | | General | [33] | Since 2014 |
| OPR series | USA | Not clear | Own Agglutinates (OPR-H/L 2W) | General | [36] | Since 2015 |

| | | | | | | |
|---|---|---|---|---|---|---|
| GSC-1 | USA | No | | General | [37] | 2008 |
| NU-LHT/1M/2M/3M/2C/1D | USA | | Pseudo-agglutinate and "good" glass | General | [38] | 2009 |
| OB-1 | Canada | | Fayalitic olivine slag glass | General | [39] | 2008 |
| CHENOBI | Canada | | Glassy component from plasma-melted Shawmere anorthosite | General | [40] | 2009 |
| CAS-1 Chinese Academy of Sciences | China | No | | General/Geotechnical | [41] | 2009 |
| CLRS-1/2 | China | Not clear | | General | [23,33] | 2009 |
| NEU-1 Northeastern University Lunar Simulant | China | No | | General | [42] | 2017 |
| TJ-1/2 Tongji University | China | No | | General/Geotechnical | [43] | 2010 |
| BHLD20 Lunar Dust Simulant | China | No | Glassy component from material partially melted in a muffle furnace | General | [44] | 2017 |
| CLDS-i | China | Yes | | General/Toxicological | [45] | 2016 |
| NAO-1 National Astronomical Observatories | China | No | | General | [46] | 2009 |
| Oshima Simulant | Japan | No | | General | [47] | 2008 |
| FJS-1/2/3 Fuji Japanese Simulant | Japan | No | | General | [48,49] | 1998 |
| Kohyama Simulant | Japan | No | | General | [47] | 2008 |
| DNA-1 De NoAntri | Italy | No | | General/3D printing | [50] | 2014 |

* Either year of publication or of the first available technical data.

# 2. MATERIALS AND METHODS

## 2.1 Chemicals and Materials Synthesis

Carlo Erba (Italy) reagent grade chemicals were used.

4A zeolite (framework type LTA, $Na_{12}Al_{12}Si_{12}O_{48}\cdot 27H_2O$, hereafter referred to as "Na-A zeolite") and 13X zeolite (framework type FAU, $Na_{86}Al_{86}Si_{106}O_{384}\cdot 264H_2O$, hereafter referred to as "Na-X zeolite") were used as parent zeolites. Their cation exchange capacity was determined by the "batch exchange method"[51,52] and was very close to the calculated cation exchange capacity of Na-A and Na-X zeolite, *i.e.* 5.48 and 4.73 meq $g^{-1}$, respectively.

Scheme 1 shows the adopted preparation procedure: the parent zeolite was contacted with a 0.1 M $Fe^{2+}$ solution, prepared by dissolving $FeSO_4\cdot 7H_2O$ (99.5 wt. %) in doubly distilled water (solid/liquid weight ratio = 1/50 g/g; contact time $t$ = 40 min). To prevent $Fe^{2+}$ oxidation, the temperature was kept at about 280 K and Ar was continuously bubbled into the solution.[53] The solid was then recovered by filtration and contacted again with a fresh solution: this step was repeated 8 and 5 times with Na-A and Na-X zeolite, respectively, due to their different exchange capacity.[54,55] The

resulting powders were washed with doubly distilled water, dried for about one day at 353 K and eventually stored for at least 3 days in a 50% relative humidity environment, to allow water saturation of the zeolite. Afterwards, the $Fe^{2+}$ exchanged zeolites (hereafter referred to as Fe-A and Fe-X zeolite) were treated in a Pt crucible at 1023 K for 2 h (heating rate 10 degrees $min^{-1}$) by flowing a 2 vol.% $H_2$ in Ar mixture inside an $Al_2O_3$ tubular furnace (inner diameter = 6.9 cm, height = 91 cm). Afterwards, the furnace was switched off and the samples were left to cool down to room temperature. The two nanocomposites from the Na-A and Na-X zeolites will be hereafter referred to as SMA_A and SMA_X, respectively (SMA = Simulated Moon Agglutinate).

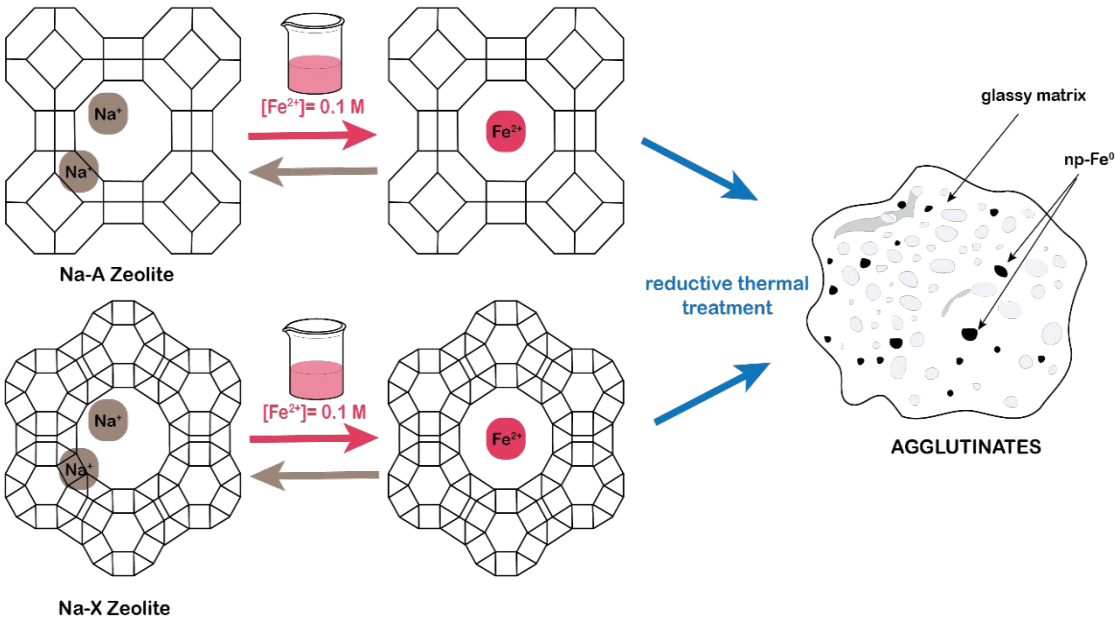

**Scheme 1**: Sketch (not in scale) of the preparation procedure of both SMA_A and SMA_X nanocomposites by $Fe^{2+}$ exchange of either Na-A or Na-X zeolite and successive reductive thermal treatment at 1073 K.

## 2.2 Characterization Methods

The $Fe^{2+}$ and (residual) $Na^{+}$ contents of both Fe-A and Fe-X zeolites were determined by atomic absorption spectrophotometry (AAS, Perkin-Elmer Analyst 100 apparatus) after dissolving the solids in a 40 wt.% HF and 14 wt.% $HClO_4$ aqueous solution.[56,57]

The powder materials were characterized by X-ray powder diffraction (XRPD) on a Philips X'Pert diffractometer equipped with a Cu $K_\alpha$ radiation ($\lambda$ = 1.5406 Å; 2$\theta$ range = 5° - 100°; step = 0.02° 2$\theta$; time per step = 1 s); phases identification was performed by referring to the PDF-2 Release 2002 database. The full-profile Rietveld method was applied to the diffraction patterns, with $LaB_6$ powder as internal standard (to evaluate crystalline and/or amorphous phases) and by using the High Score Plus v 3.0e software (Malvern Panalytical).

$N_2$ adsorption/desorption isotherms at 77 K were measured on samples previously outgassed at 523 K for 4 h to remove water and other atmospheric contaminants (Quantachrome Autosorb 1 instrument). The samples specific surface area was calculated according to the Brunauer–Emmett–Teller (BET) method ($S_{BET}$); total pore volume ($V_p$) and micropore volume ($V_{mp}$) were determined from the amount of adsorbed $N_2$ at $P/P_0$ = 0.9 and according to the *t*-plot method, respectively (see Table 2).

Transmission electron microscopy (TEM) analysis was carried out on a JEOL 3010-UHR instrument operating at 300 kV and a FEI-TECNAI instrument operating at 120 kV, both equipped with $LaB_6$ filaments. To obtain a good dispersion, the powders were either briefly contacted with lacey carbon Cu grids (resulting in the mere electrostatic adhesion of some particles to the sample holder), or pre-dispersed in ethanol and, then, dropped on carbon Cu grids. Average size of np-$Fe^0$ was obtained by considering more than 100 particles on the TEM images (at least 5 different images).

Differential centrifugal sedimentation method was applied to calculate the particle size distribution on a CPS Disc Centrifuge: before the measurements, the powders were dispersed in water and sonicated for 5 min.

### 2.3 Magnetic and electrical properties measurement

The magnetic properties of the SMA_A and SMA_X nanocomposites were studied at both room temperature and 5 K (low T) on a SQUID magnetometer operating in the 0-70 kOe range. The FC/ZFC curves of the magnetic nanocomposites were obtained under a field of 200 Oe in the temperature interval 10-300 K using the Lakeshore VSM.

The electrical properties of the nanocomposites were studied using Broadband Dielectric Spectroscopy (BDS) and DC conductivity measurements techniques.[58,59] In both types of measurement, samples made of dust layers were approximately 200 μm thick and confined between two metallic electrodes. Isotherm dielectric spectroscopy measurements were carried out under dry $N_2$ flow at atmospheric pressure at the CIRIMAT laboratory (Toulouse, France) in the 133 - 423 K temperature range and in the

$10^{-2}$ -$10^{6}$ Hz frequency range. By steps of 283 K, sinusoidal voltages $U^*$ (amplitude 1V, 10 points per frequency decade) were isothermally applied to the sample. The measurements of both the induced current ($I^*$) and its phase shift relative to the applied voltage yielded the complex impedance ($Z^*$) values as a function of temperature and frequency. The complex dielectric permittivity $\varepsilon^*$ (equation (1)) and electrical conductivity

$$\varepsilon^*(\omega) = \varepsilon'(\omega) - i\varepsilon''(\omega) = \frac{1}{i\omega C_0 Z^*(\omega)} \quad (1.1)$$

$$C_0 = \frac{\varepsilon_0 A}{l} \quad (1.2)$$

$\sigma^*$ (equation (2)) formalisms were used to represent the BDS data.

where $\varepsilon$' and $\varepsilon$'' are the real and imaginary parts of $\varepsilon^*$, $\omega$ the angular frequency, and $C_0$ the capacitance of the vacuum-filled capacitor formed by the two electrodes of area A

$$\sigma^*(\omega) = \sigma'(\omega) + i\sigma''(\omega) = i\omega\varepsilon_0\varepsilon^*(\omega) \quad (2)$$

separated by the sample thickness l ($\varepsilon_0$ is the vacuum permittivity), where $\sigma$' and $\sigma$'' are the real and imaginary parts of $\sigma^*$.

DC conductivity measurements were carried out under secondary vacuum (< $10^{-6}$ mbar) at the ONERA laboratory (Toulouse, France) with a constant voltage between the electrodes and with temperature from 298 to 423 K. Dust layer density was around 0.6 g $cm^{-3}$.

# 3. Results and Discussion

## 3.1 Physico-chemical characterization

As determined by AAS analysis, the Fe-A zeolite contains 4.51 meq $g^{-1}$ $Fe^{2+}$ and 0.58 meq $g^{-1}$ $Na^+$, and the Fe-X zeolite contains 3.54 meq $g^{-1}$ $Fe^{2+}$ and 1.15 meq $g^{-1}$ $Na^+$. The corresponding cation equivalent fractions were calculated as $x_{Fe}$ = 0.89 and $x_{Na}$ = 0.11 (Fe-A), and $x_{Fe}$ = 0.75 and $x_{Na}$ = 0.25 (Fe-X). The wt. % Fe was 16.9 and 13.1 wt. % in SMA_A and SMA_X, respectively, as calculated from the $Fe^{2+}$ content of the $Fe^{2+}$-exchanged zeolites by considering the nanocomposites as completely dehydrated

materials. The different iron content in the two $Fe^{2+}$- exchanged zeolites is probably determined by their different cation exchange capacity, open windows, cage size and pore structure: Na-A has, indeed, larger cation exchange capacity (5.48 meq $g^{-1}$) and smaller pore window (0.41 nm) than Na-X (4.74 meq $g^{-1}$ and 0.74 nm).

Figure 1 reports the XRD patterns of i) the parent Na-A and Na-X zeolites; ii) the $Fe^{2+}$exchanged ones (Fe-A and Fe-X) and iii) the nanocomposites (SMA_A and SMA_X). Comparison between the XRD patterns of the parent zeolites and the $Fe^{2+}$-exchanged ones shows: i) a slight shift of some diffraction peaks towards larger $2\theta$ angles; ii) a decrease of the intensity of most of the peaks and iii) an increase of the intensity of some minor peaks in Fe-A and Fe-X XRD patterns. Such findings may be reasonably ascribed to small changes of the zeolite unit cell volume upon $Fe^{2+}$ exchange and/or to a larger X-ray absorption coefficient of $Fe^{2+}$ ions, as previously found with $Ba^{2+}$ exchanged A zeolite.[60]

In the XRD patterns of both SMA_A and SMA_X, the sharp peak at 44.6 $2\theta$ is ascribed to the most intense diffraction of $\alpha$-$Fe^0$ phase ($d_{011}$), whereas the broad signal centered at about 24 $2\theta$ is due to the occurrence of an amorphous phase. Some broad

(and weak) peaks ascribable to residual parent zeolite are only detected with the SMA_A pattern (being instead absent with SMA_X) along with two peaks at *ca.* 35.8 2θ and 31.6 2θ (asterisks) that are assigned to the two most intense diffractions ($d_{121}$ and $d_{301}$) of fayalite ($Fe_2SiO_4$, *vide infra*).

As confirmed by XRD results, during the reductive thermal treatment, $Fe^{2+}$ cations are reduced to their zero-valent state, while the zeolite framework releases oxygen with formation of water vapor and consequent collapse of the microporous crystalline structure (eq. 3): [31]

$$Fe^{2+}{\cdot}O_{zeo} + H_{2(g)} \rightarrow Fe_{(s)} + H_2O_{(g)} \qquad (3)$$

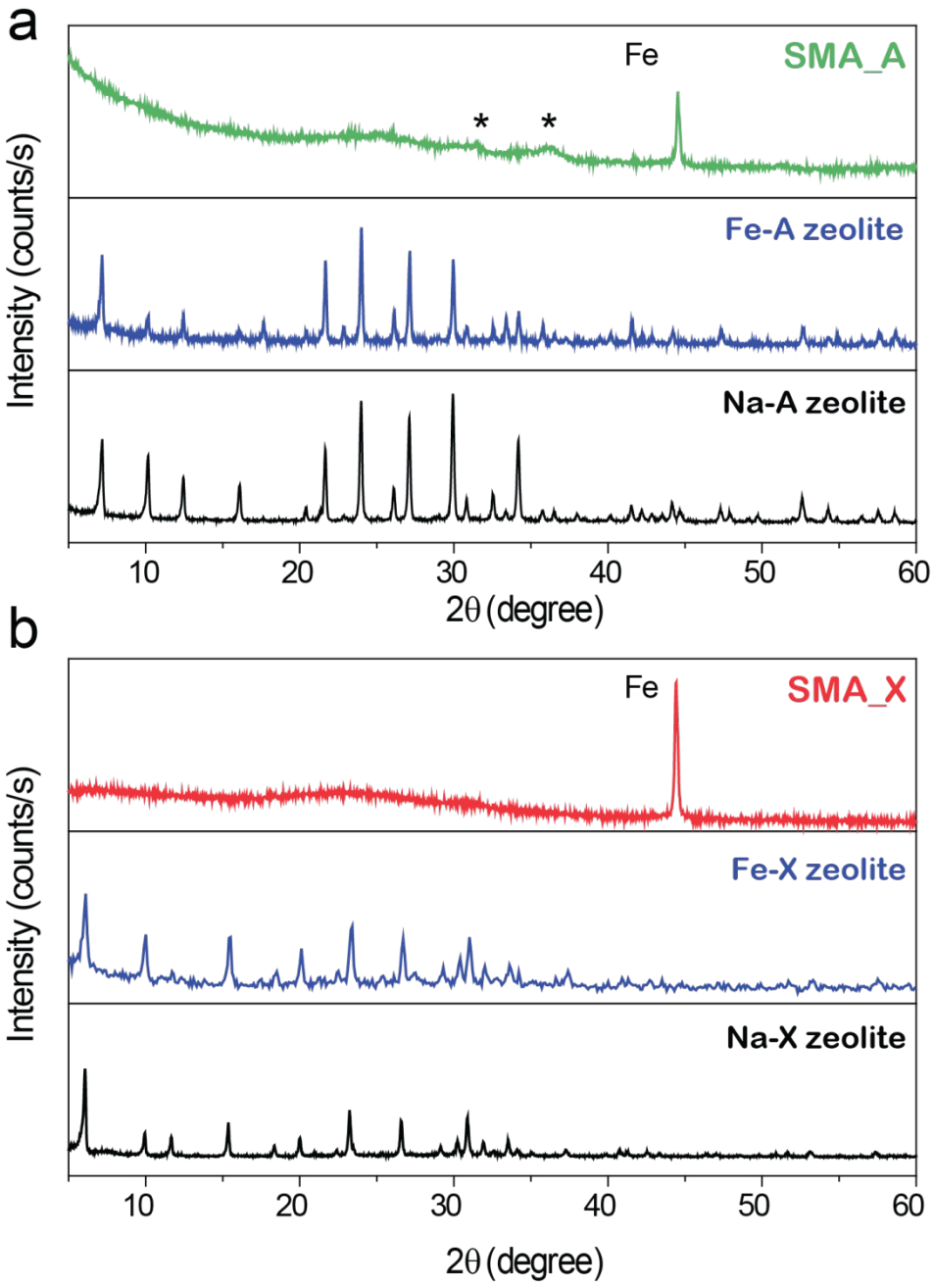


**Figure 1.** Section a: XRD patterns of Na-A (black curve); Fe-A (blue curve) and SMA_A (green curve; asterisks: diffraction peaks assigned to fayalite). Section b: powder XRD patterns of Na-X (black curve); Fe-X (blue curve) and SMA_X (red curve).

Quantitative phase analysis (QPA) results, as obtained by the Rietveld method, are reported in Table 2: the reductive thermal treatment was unable to reduce all the iron occurring in the exchanged zeolites (16.9 and 13.1 wt.%, respectively), in that the amount of $Fe^0$ in the nanocomposites was 2.6 wt.% (SMA_A) and 1.6 wt.% (SMA_X), the remaining iron mainly occurring in the amorphous phase (89.4 and 98.4 wt.%, respectively) resulting from the zeolite thermal collapse. The QPA showed that, with respect to SMA_X, a smaller amount of amorphous phase was found with SMA_A, in which also small amounts of parent zeolite (1.0 wt.%) and of fayalite ($Fe_2SiO_4$, 7.0 wt.%) were present.

The higher amount of $Fe^0$ in the SMA_A nanocomposite is in agreement with previous work concerning similar nanocomposites obtained by thermal reduction of $Ni^{2+}$-exchanged A and X zeolites.[61] Comparable results were, indeed, obtained, in that QPA showed the occurrence of some residual zeolite in the A zeolite-derived nanocomposites, where the reduction of $Ni^{2+}$ species was more extensive than in X zeolite-derived ones. On the ground of those results, the higher $Fe^0$ content in SMA_A

is ascribed to a more facile reduction of the transition metal ions in the A zeolite structure.

**Table 2**: Results of QPA as obtained by Rietveld refinement (phase wt. %). Specific surface area ($S_{BET}$); total pore volume ($V_p$); micropore volume ($V_{mp}$), as obtained by $N_2$ isotherms at 77 K.

| | Parent Zeolite (wt. %) | $Fe^0$ (wt. %) | $Fe_2SiO_4$ (wt. %) | Amorphous phase (wt. %) | $S_{BET}$ ($m^2\ g^{-1}$) | $V_p$ ($cm^3\ g^{-1}$) | $V_{mp}$ ($cm^3\ g^{-1}$) |
|---|---|---|---|---|---|---|---|
| SMA_A | 1.0[31] | 2.6[31] | 7.0[31] | 89.4[31] | 9.50 | 0.055 | 0.007 |
| SMA_X | - | 1.6 | - | 98.4 | 19.03 | 0.066 | 0.029 |

The zeolite structure collapse is confirmed by the values of specific surface area ($S_{BET}$), total pore volume ($V_p$) and micropore volume ($V_{mp}$) (Table 2) obtained from the $N_2$ isotherms at 77 K (not reported): the low surface and porosity of the two nanocomposites ($S_{BET}$ values of SMA_A and SMA_X are two orders of magnitude smaller than those of the parent zeolites) reflect the occurrence of a densification

phenomenon due to zeolite collapse, which should also affect the grain size. Figure 2 reports the corresponding grain size distributions: the normalized distribution of SMA_A (green curve) shows two maxima of similar intensity at about 4.5 and 10 μm, with 50 wt.% grains smaller than 6.1 μm (dotted green curve), whereas the normalized distribution of SMA_X (red curve) shows only one peak at about 3.5 μm, with 50 wt.% grains smaller than 3.8 μm (dotted red curve). The parent zeolites had larger average grain size (*ca.* 10-12 μm)[62,63] than the nanocomposites, which indeed show grain size similar to that of the lunar soil coarse fraction (2.5-10 μm), but still larger than that of the fine (0.1-2.5 μm) and ultra-fine (< 0.1 μm) fractions. For studies requiring smaller grain size (for instance, the breathable, and thus dangerous, fraction with aerodynamic diameter < 10 μm)[6,7] proper ball-milling procedures applied to the present nanocomposites could allow decreasing the grain size down to 300 nm.[64]

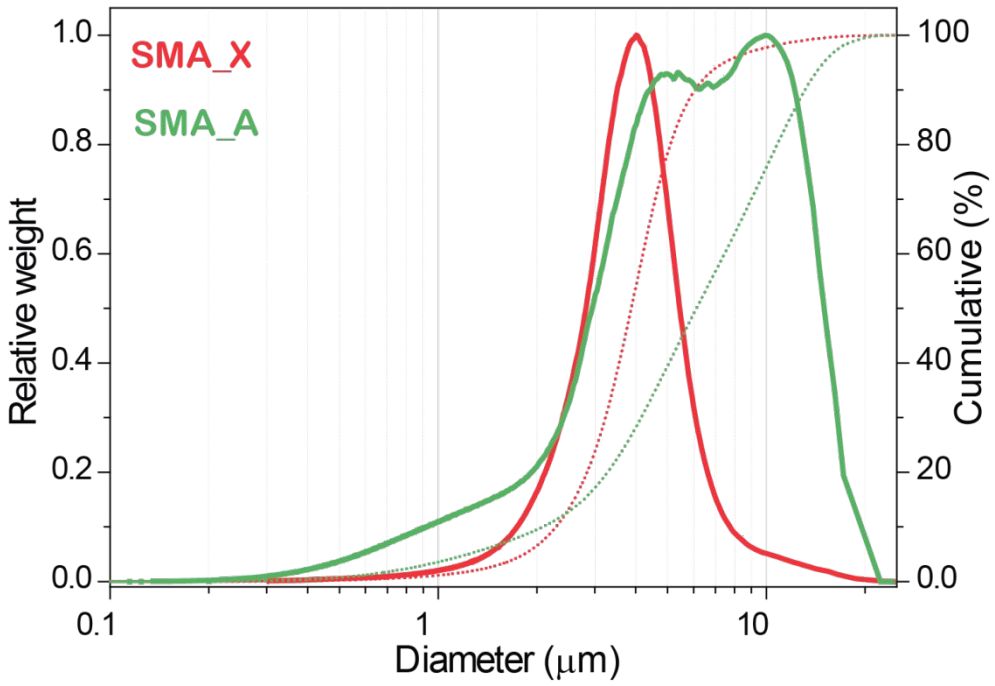


**Figure 2**: Normalized grain size distribution plots (solid curves) and cumulative curves (dotted curves) of SMA_A (green curves) and SMA_X (red curves).

The TEM images (

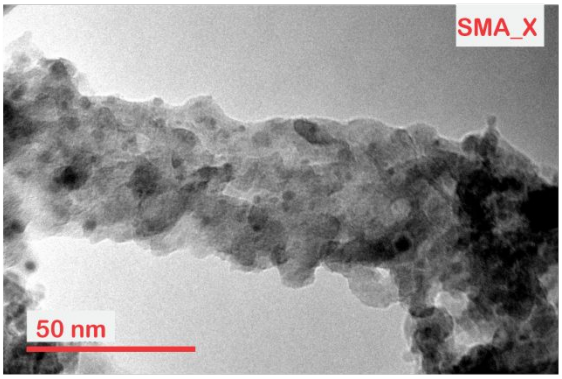


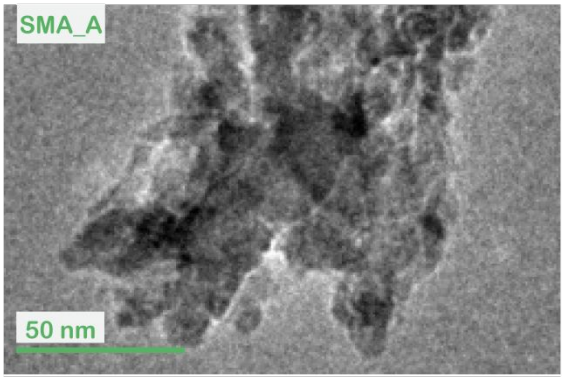

Figure 3) of the two nanocomposites show partially homogenous samples, where np-$Fe^0$ of different sizes, embedded within a glassy matrix, are detected: SMA_X shows, indeed, np-$Fe^0$ with an average diameter of 4.4 ± 1.8 nm, whereas SMA_A shows slightly larger np-$Fe^0$ (average diameter of 6 nm), as reported previously.[31] Though some larger and crystalline $Fe^0$ particles (*ca.* 50-150 nm) were also detected in both samples (not reported), both types of $Fe^0$ particles had average size compatible with the particle size distribution of $Fe^0$ globules in agglutinitic glass.[1]

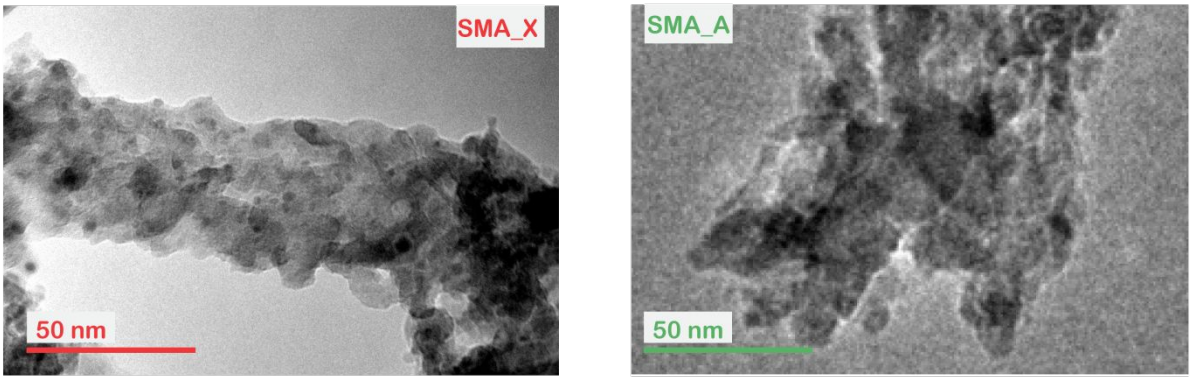


**Figure 3**: Selected TEM micrographs of SMA_X and SMA_A.

### 3.2 Magnetic and electric properties of SMA_A and SMA_X

The higher amount of $Fe^0$ in the SMA_A nanocomposite is confirmed by the results of magnetization measurements carried out at room temperature (Figure 4): SMA_A shows an extrapolated saturation magnetization $M_s$ = 9.6 emu $g^{-1}$, whereas SMA_X has $M_s$ = 7.1 emu $g^{-1}$ , with quite similar coercive fields ($H_c$ = 166Oe and 190Oe, respectively; lower inset to Figure 4). As a matter of fact, the room-temperature loops for the two nanocomposites only differ in their amplitudes (as shown in the upper inset to Figure 4, where the reduced magnetization $M/M_s$ is depicted). The similarities in coercive field, magnetic permeability, loop closure field (about 4000 Oe) and overall loop shape (including a non-saturating trend above 10 kOe) indicate that the magnetization processes are basically the same in the two nanocomposites. In particular, the magnetic signal is expected to be dominated by the contribution of large, multi-domain nanoparticles (as those of 50-150 nm size that were observed in SMA_A)[61] where the magnetization process involves domain-wall motion and magnetization rotation and determines $H_c$, low-field permeability and closure field values. The high value of $H_c$ is related to the hindrances to domain-wall motion provided by quenched-in stress in large np-$Fe^0$. On the other hand, the non-saturating behavior

of the M(H) curves is related to the magnetic response of smaller np-$Fe^0$, which were detected by TEM in SMA_A (size in the 2-10 nm range).[61] At room temperature, such nanoparticles are expected to be in the superparamagnetic phase. In principle, a non-saturating trend of the high-field magnetization could also be ascribed to a contribution from paramagnetic fayalite ($Fe_2SiO_4$); however, the maximum fayalite content (7 wt.% in SMA_A) is too small to be responsible of the observed slope of the M(H) curve at high field; moreover, no fayalite was detected in SMA_X.

Though both nanocomposites have a larger Fe content than other lunar soil simulants,[65] the magnetic properties of the SMA_A and SMA_X (Fe-rich) nanocomposites are comparable to those of the simulants, which contain large np-$Fe^0$. Typically, lunar soil is characterized by a complex magnetic behavior related to the presence of different Fe-rich compounds[66] and strongly affected by the sampling site on the Moon surface.[67] At room temperature, a quasi-superparamagnetic behavior is often observed, with coercive fields much lower than those measured in our nanocomposites,[66,68] possibly indicating that the magnetic nanoparticles have smaller

average size in actual lunar soils. The magnitude of $M_s$ in both nanocomposites is typically larger than the values measured in either lunar soils or simulants (Table 3): this is related to the amount of iron included in the diamagnetic matrix, which is higher in our nanocomposites. To this respect, the issue of the total iron content could be addressed by changing the cation exchange conditions, as the adopted preparation method allows tuning the iron content by varying, for instance, the concentration of the exchange solution and/or the parent zeolite.

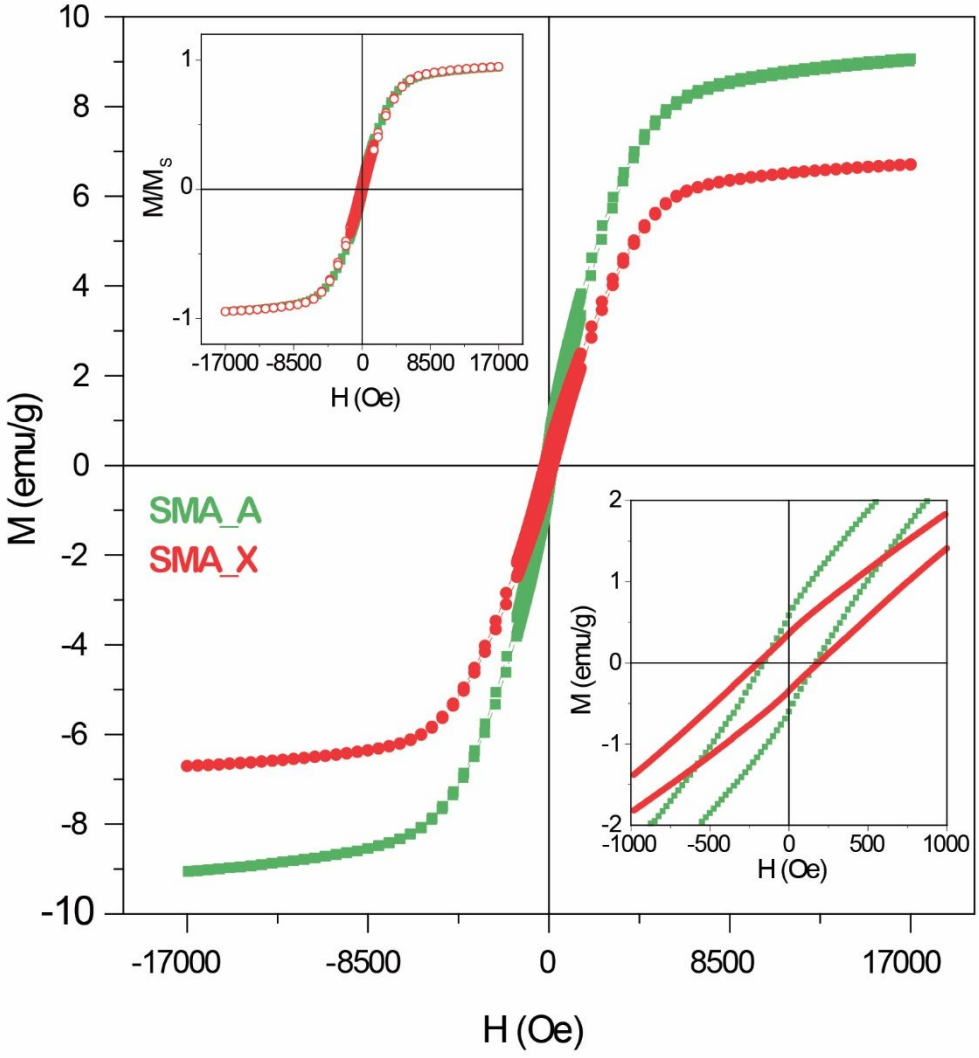


**Figure 4:** Magnetization curves at room temperature of SMA_A and SMA_X after subtraction of the diamagnetic signal from the host matrix. Upper inset: reduced ($M/M_s$) magnetization curves; lower inset: magnification of the low field region of the M(H) curves.

In view of lunar resource exploitation, it is useful to study how much does the magnetic response of the nanocomposites change as a function of temperature within the extremes measured on the Moon surface (direct *in-situ* measurements give average values of 392 K at noon and 99 K at midnight).[69] Therefore, hysteresis loops of the two nanocomposites were measured at T = 100, 200, 300, 400 K. The behavior of high-field magnetization, coercive field, high-field susceptibility is shown in Figure 5. These quantities steadily decrease with increasing temperature; the linear behavior of both $M_{17kOe}$ and $H_c$ (Figure 5a,b) is fully compatible with a high Curie temperature of multi-domain nanoparticles, whereas the non-saturating behavior of magnetization at high fields, measured by the high-field susceptibility (Figure 5c), is simply explained in terms of field-induced ordering of surface magnetization states rather than in terms of superparamagnetic contribution from the smaller particles: in the latter case, the slope of the M(H) curve should change much more than what actually observed between 100 and 400 K. In any case, the measured differences in magnetic properties of lunar soil between day and night are truly remarkable: this should be taken into account in the

design and the fabrication of sensors/actuators based on the detection or influenced by the stray magnetic fields generated from lunar soil.

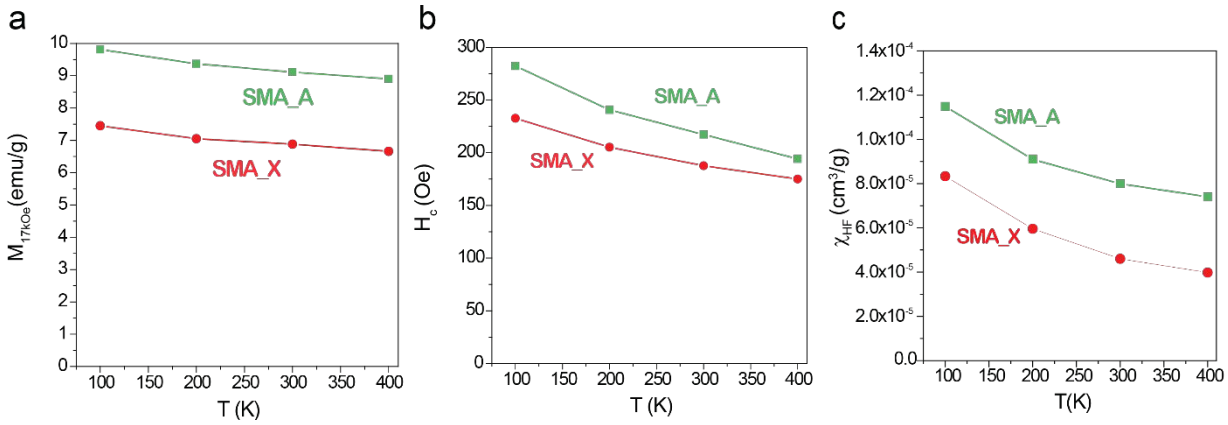


**Figure 5:** (a) Temperature behavior of high field magnetization, (b) coercive field and (c) high-field susceptibility in SMA_A (green curves) and SMA_X (red curves).

The relative permittivity and loss tangent as a function of frequency obtained by BDS at various temperatures are shown in Figure 6. For frequencies higher than $10^{-2}$ Hz, the relative permittivity varies from 3 to 3.3 between 133 K and 423 K for SMA_A and from 3.2 to 3.4 between 143 K and 423 K for SMA_X.

A relative permittivity of 3 is expected for lunar samples.[70] Lunar sample 14163,131 exhibited a permittivity of approximately 2.4 over a frequency range of $10^2$-$10^5$ Hz. Here, at low frequencies and high temperatures, a sharp increase in the relative permittivity of both SMA_A and SMA_X is observed, which is ascribed to the accumulation of electrical charge carriers either around the particles (Maxwell-Wagner-Sillars phenomenon)[71,72] or at the sample/electrode interfaces (electrode polarization effect).[73] Such accumulation is possible at high temperatures due to an increase in conductivity, leading to the formation of macro-dipoles that are able to preferentially align along the electric field lines only at low frequencies. The loss tangent quantifies the dissipation of energy of dielectric materials. It is constant above 1 Hz, for both SMA_A and SMA_X, and it varies with temperature between 0.003 to almost 0.1 for SMA_A and between 0.002 and 0.3 for SMA_X, in the studied temperature range. More precisely, at ambient temperature, the loss tangent is 0.01-0.02 and 0.006-0.008 for SMA_A and SMA_X, respectively. In comparison, the loss tangent of lunar sample 14163,131 varies between 0.05 and 0.001 at room temperature in the $10^{2}$-$10^4$ Hz frequency range.[58]

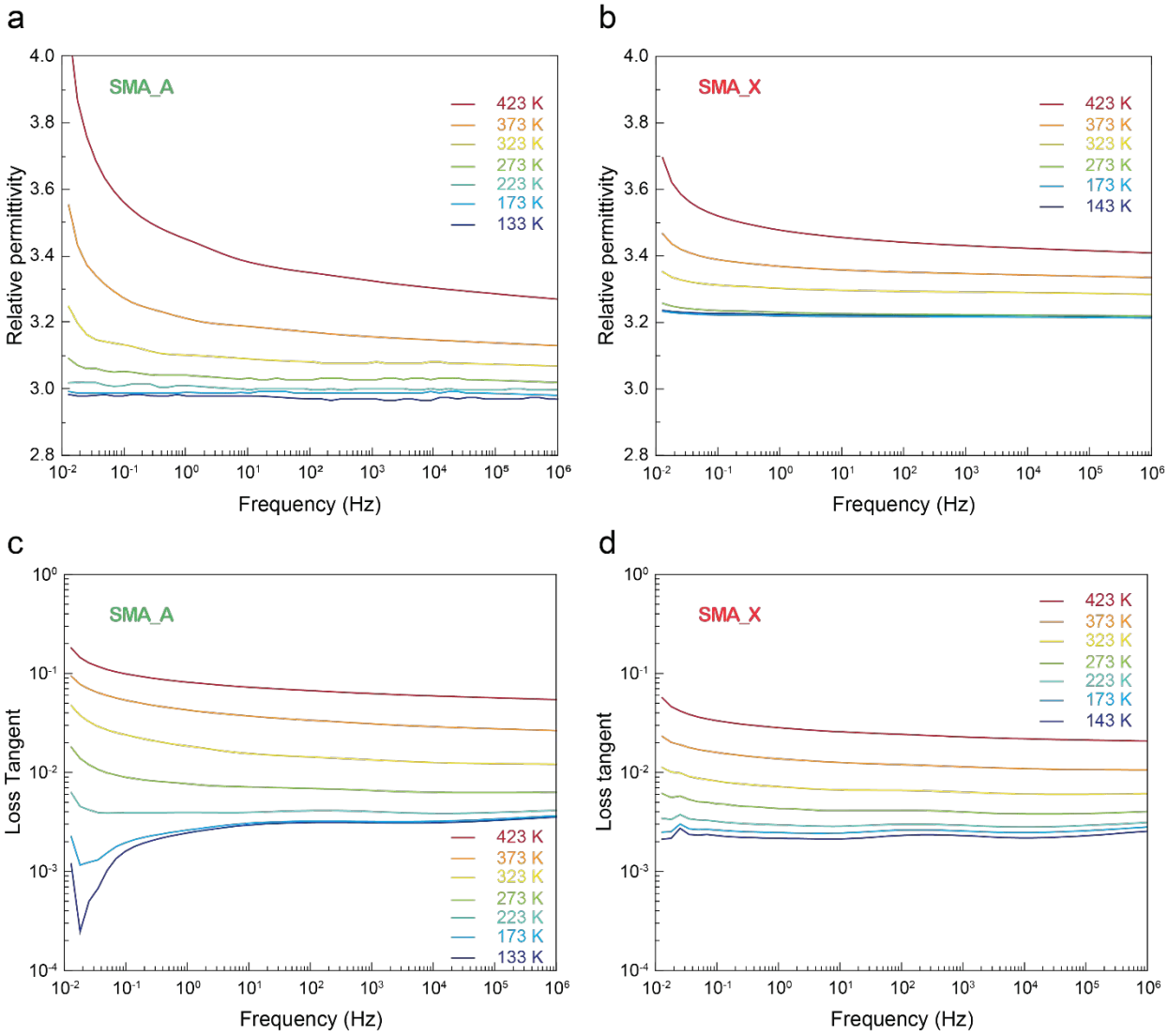


**Figure 6** (a) Isothermal relative permittivity spectra of SMA_A; (b) isothermal relative permittivity spectra of SMA_X; (c) isothermal loss tangent spectra of SMA_A; (d) isothermal loss tangent spectra of SMA_X.

Figure 7 shows the isothermal electrical conductivity spectra of SMA_A (section a) and SMA_X (section b). BDS electrical conductivity shows the so-called universal power law behavior typical of disordered dielectrics.[74] The conductivity follows a power-

$$\sigma' = \sigma_{DC} + A\omega^n,\ 0 < n < 1 \qquad (4)$$

like trend that can be described by eq. (4)

where σ' is the conductivity, $\sigma_{DC}$ is the frequency-independent DC conductivity, A is a constant and ω the angular pulsation. At higher temperatures and lower frequencies, $\sigma_{DC}$ plateaus are observed, independent of frequency, which are representative of carrier-free transport. They are reached approximately above 293 K and 353 K for SMA_A and SMA_X, respectively. At lower temperatures, the transition to DC plateaus is expected at frequencies below the lower limit of the BDS range. The $\sigma_{DC}$ component of SMA_A at 293 K can be approximated by the value of σ' at 0.01 Hz, i.e. $10^{-10}$ S $m^{-1}$.

The $\sigma_{DC}$ component of SMA_X cannot be extracted at 293 K from this experiment since no plateau is reached at 0.01 Hz.

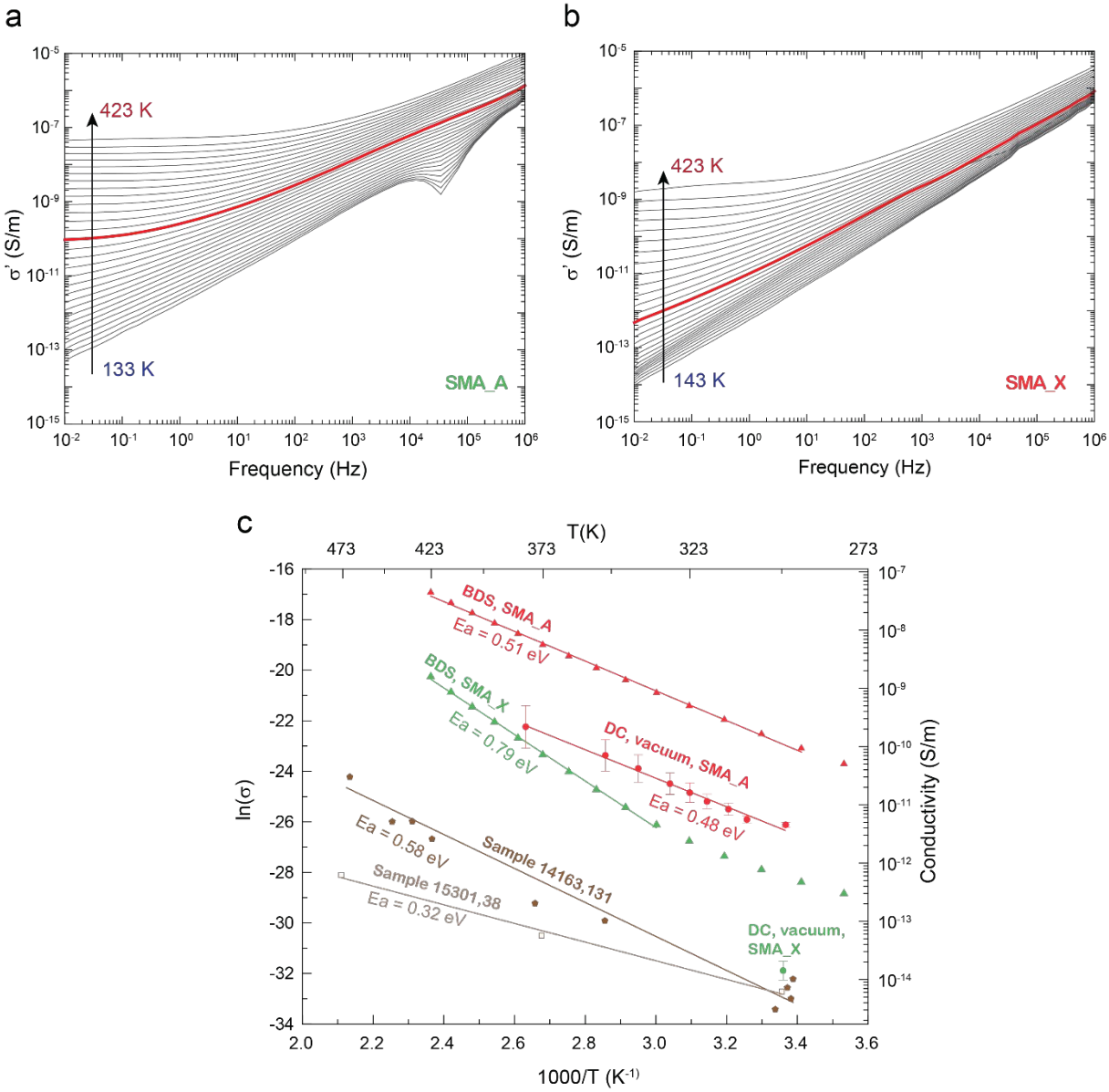


**Figure 7.** Isothermal electrical conductivity spectra of SMA_A (a) and SMA_X (b) (measurements at 293 K are reported as red curves). (c) Arrhenius diagrams of SMA_A

and SMA_X as obtained by BDS and DC techniques. The BDS curves correspond to the DC plateaus (measured at 0.01 Hz). Conductivities mesurements done on 14163,131 and 15301,38 samples are also reported as comparison.[58,75]

Figure 7c shows the trend of σ' at 0.01 Hz as a function of temperature, as obtained by BDS. The electrical conductivity follows an Arrhenius law (eq. (5), where $E_a$ is the activation energy, $k_B$ the Boltzmann constant, T the temperature and $\sigma_\infty$ a pre-exponential factor)) approximately above 293 K and 353 K for SMA_A and SMA_X, respectively:

$$\sigma_{DC}(T)=\sigma_\infty \exp(-E_a/(k_B T)) \qquad (5)$$

The activation energy $E_a$ of SMA_A and SMA_X is approximately 0.5 eV and 0.8 eV, respectively: SMA_A is *ca.* two orders of magnitude more conductive than SMA_X, possibly in relation to the different iron content.

As for DC measurements, SMA_A also follows an Arrhenius law above 293 K with activation energy of 0.5 eV. Further tests show a slight increase in the DC conductivity under nitrogen with respect to vacuum. The DC conductivity of SMA_A under vacuum at 293 K ranges between $5\times10^{-12}$ and $1\times10^{-11}$ S m$^{-1}$, *i.e.* about one order of magnitude lower than the DC conductivity determined from BDS measurements performed at 0.01 Hz. Obtained SMA_X results are also presented, but due to long relaxation time (SMA_X being much less conductive than SMA_A), the DC-conductivity value can only be obtained at room temperature. Electrical DC-conductivity of SMA_X is about $1.4\text{x}10^{-14}$ S m$^{-1}$ and the BDS activation energy is 0.8 eV. Considering the high complexity of charge transport through a dust layer, as well as the set of experimental parameters that are very difficult to repeat from one facility to another (*e.g.* vacuum vs nitrogen, dust packing and electrical contacts), a factor of several tens between BDS and DC results is satisfactory.

For comparison, in Figure 7c the electrical conductivities of lunar samples 14163,131 and 15301,38 are also reported. Under vacuum, conductivity of lunar sample 14163,131 ranges from $0.2\times10^{-14}$ to $1.0\times10^{-14}$ S m$^{-1}$ at 298 K to $10^{-10}$ S m$^{-1}$ at 523 K[58]

and conductivity of 15301,38 sample ranges from 6,2.$10^{-15}$ S $m^{-1}$ at 298 K to 6,2.$10^{-13}$ S $m^{-1}$ at 473 K.[76] As for SMA_A and SMA_X nanocomposites, both lunar samples follow an Arrhenius law for temperatures ranging from 298 K to 473 K. Activation energy of 14163,131 sample ranges from 0.4 to 0.9 eV.[58] Our numerical estimation of activation energy of 14163,131 and 15301,38 samples is 0.6 and 0.3 eV, respectively, which is in line with published data for 14163,131 sample, from 0.4 to 0.9 eV.[58]

At 298 K, 14163,131 and 15301,38 samples have an average conductivity of 6.2x$10^{-15}$ S $m^{-1}$. BDS and DC measurements of SMA_A simulant are respectively four and three orders of magnitude higher than values from literature. DC-conductivity value of SMA_X nanocomposite is higher than the average conductivity by a factor of 2.

Electrical properties of lunar dust can vary from a region to another: for instance, sample 14163, 131 was collected during the Apollo 14 mission and is described as a "soil sample", *i.e.* composed of both dusts and very small rocks.[77] At 298 K, under vacuum, the electrical conductivity of the 14163,131 sample is around $10^{-15}$-$10^{-14}$ S $m^{-1}$ and strongly depends on temperature. A correlation between the electrical conductivity and the iron content of a sample was found.[78] The higher conductivity of SMA_A with

respect to the one measured on the 14163,131 and 15301,38 lunar samples could be ascribed to the higher iron content of SMA_A. The chemical composition of sample 14163,131 is ~ 10 wt.% FeO[79] and 15301,38 is ~ wt.% FeO.[80] To this respect, the proposed synthesis method may be properly tuned in order to vary the type and amount of phases (*i.e.* $Fe^0$ and FeO) present in our nanocomposites, by changing, for instance, temperature and duration of the reductive thermal treatment.[61]

As a whole, the DC-conductivity value of SMA_X is very close to literature values and thus, from the electrical point of view, SMA_X is representative of the electrical properties of lunar samples. Another point that should be stressed is that the grains of SMA samples are smaller than 25 μm, whereas 14163,131 and 15301,38 samples have a particle mean size of 73 and 65 μm, respectively. This should be also considered while evaluating the conductivity values.

However, on the ground of the literature and of the physico-chemical characterization of SMA_A and SMA_X nanocomposites, they should not be considered lunar simulants as such, but could be mixed to other simulants to obtain a composition as close as possible to the various typologies of actual lunar samples.

**Table 3**: Room-temperature values of typical magnetic and electric properties of the SMA_A and SMA_X nanocomposites, as compared to the ones actually measured on lunar samples and reported by the literature.

| Property / Material | $M_s$ (emu/g) | $M_r$ (emu/g) | $H_c$ (Oe) | σ(S/m) ~293 K | | Ea (eV) | | Ref. |
|---|---|---|---|---|---|---|---|---|
| | | | | BDS | DC | BDS | DC | |
| **SMA_A** | 9.1 | 0.64 | 217 | $\sim 10^{-10}$ | $\sim 5.10^{-12}$ | 0.51 | 0.48 | this work |
| **SMA_X** | 6.9 | 0.34 | 188 | (1) | $\sim 1.4.10^{-14}$ | 0.79 | (2) | this work |
| **Lunar fines (# 10084-89)** | 1.27 | $8.4 \times 10^{-2}$ | 36 | | | | | 66 |
| **Lunar microbreccia (#10088)** | 0.44 | $6.7 \times 10^{-2}$ | 125 | | | | | 66 |
| **Small soils (min/max)** | 2-2.2 | 0.10-0.46 | Not available | | | | | 67 |
| **Breccia** | 2 | 0.11 | 62 | | | | | 67 |
| **Soils (min/max)** | 0.20-1.70 | $1.4 \times 10^{-2}$-0.46 | 18-88 | | | | | 67 |
| **A17 soils (min/max)** | 0.125 – 15.15 | $9 \times 10^{-3}$ – 0.95 | 8-94 | | | | | 68 |
| **A14 soil 14163,131** | | | | $10^{-15}$-$10^{-14}$ | | 0.4-0.9 (0.58) | | 58 |
| **A15 soil 15301,38** | | | | $6.2.10^{-15}$ | | 0.32 | | 76 |

(1)DC-conductivity plateaus were not reached at 293 K

(2) Not enough data to provide information.

# 4. Conclusions

Two nanocomposites containing $Fe^0$ nanoparticles embedded in a glassy matrix were obtained by means of an efficient, inexpensive and scalable synthesis method. Both nanocomposites showed proper physico-chemical properties to be considered as suitable materials to simulate the agglutinitic fraction of regolith, lacking in most of lunar simulants. The so-obtained simulated Moon agglutinates (SMA) nanocomposites should not be used as such, but, if added to available simulants, could fill the gap with respect to actual lunar regolith/soil.

In particular, a thorough characterization of the nanocomposites' magnetic and electric properties showed their potential application in the field of lunar simulants, due to the strong correlation between the $Fe^0$ content and their magnetic and electric behavior. The nanocomposite obtained by thermal treatment under reducing atmosphere of $Fe^{2+}$-exchanged X zeolite (SMA_X), which contains a smaller $Fe^0$ content (1.6 wt.%), exhibited values of both electrical and magnetic quantities very close to those of real lunar samples. The magnetic properties of the simulated Moon agglutinates resulted to be markedly affected by temperature and thus could largely change in the

lunar night/day succession, as it is expected to occur with the magnetic components of actual lunar regolith/soil.

Nonetheless, the versatility and tuneability of the proposed preparation method allows improving further the properties of the final nanocomposites, by operating on the main key parameters of the process, i.e. the cation exchange procedure, the type of parent zeolite, the temperature and duration of the reducing thermal treatment and the (possible) ball milling procedure in order to reduce the grain size. As far as the parent zeolite is concerned, future work will consider zeolites with higher Si/Al ratio, in order to have a smaller final Fe content. Moreover, as the plagioclase component of the lunar regolith is rich in Ca-containing mineral (*e.g.* anorthite), the use of Ca-containing zeolites as parent material could be a further effort towards the production of lunar regolith/soil simulants. Indeed, some Ca-containing natural zeolites (like clinoptilolite, chabazite or phillipsite) are available at a low cost and could be used as parent materials: besides the presence of Ca, their higher Si/Al ratio is typical of lunar minerals and would allow obtaining nanocomposites with comparable iron content, as well.

## Acknowledgment

Financial support by ALFED S.P.A. is acknowledged. The authors thank Giulia di Francesco for Particle Size Analysis with Differential Centrifugal Sedimentation in Prof. Sethi's group (Department of Environment, Land and Infrastructure Engineering, Politecnico di Torino) and Dr Michelangelo Polisi for kindly providing some references for Rietveld refinement.

## References

(1) Liu, Y.; Taylor, L. A. Characterization of Lunar Dust and a Synopsis of Available Lunar Simulants. *Planet. Space Sci.* **2011**, *59* (14), 1769–1783.

(2) Wallace, W. T.; Lawrence, T. A.; Liu, Y.; Bonnie, C. L. .; David, M. S. .; Chen, B.; Antony, J. S. . Lunar Dust and Lunar Simulant Activation and Monitoring. *Meteorit. Planet. Sci.* **2009**, *44* (7), 961–970.

(3) Carpenter, J. D.; Fisackerly, R.; De Rosa, D.; Houdou, B. Scientific Preparations for Lunar Exploration with the European Lunar Lander. *Planet. Space Sci.* **2013**, *74* (1), 208–223.

(4) Spray, J. G. Generation of a Lunar Regolith Agglutinate Simulant Using Friction Welding Apparatus. *Planet. Space Sci.* **2010**, *58* (14–15), 1771–1774.

(5) Khan-Mayberry, N. The Lunar Environment: Determining the Health Effects of Exposure to Moon Dusts. *Acta Astronaut.* **2008**, *63* (7), 1006–1014.

(6) Zhang, J.; Yang, W.; Hu, S.; Lin, Y.; Fang, G.; Li, C.; Peng, W.; Zhu, S.; He, Z.; Zhou, B.; et al. Volcanic History of the Imbrium Basin: A Close-up View from the Lunar Rover Yutu. *Proc. Natl. Acad. Sci.* **2015**, *112* (17), 5342–5347.

(7) Spray, J. G. Lithification Mechanisms for Planetary Regoliths: The Glue That

Binds. *Annu. Rev. Earth Planet. Sci.* **2016**, *44*, 139–174.

(8) McKay, D. S.; Heiken, G.; Basu, A.; Blanford, G.; Simon, S.; Reedy, R.; French, B. M.; Papike, J. The Lunar Regolith. In *Lunar Sourcebook: a user's guide to the moon*; Heiken, G. H., Vaniman, D. T., French, B. M., Eds.; Press Syndicate of the University of Cambridge: New York, 1991; pp 285–356.

(9) Lucey, P.; Korotev, R. L.; Gillis, J. J.; Taylor, L. A.; Lawrence, D.; Campbell, B. A.; Elphic, R.; Feldman, B.; Hood, L. L.; Hunten, D.; et al. Understanding the Lunar Surface and Space-Moon Interactions. *Rev. Miner. Geochem.* **2006**, *60*, 83–219.

(10) Liu, Y.; Park, J.; Schnare, D. W.; Hill, E.; Taylor, L. A. Characterization of Lunar Dust for Toxicological Studies. II: Texture and Shape Characteristic. *J. Aerosp. Eng.* **2008**, *21* (4), 272–279.

(11) Park, J.; Liu, Y.; Kihm, K. D.; Taylor, L. A. Characterization of Lunar Dust for Toxicological Studies. I: Particle Size Distribution. *J. Aerosp. Eng.* **2008**, *21* (4), 266–271.

(12) Colwell, J. E.; Batiste, S.; Horányi, M.; Robertson, S.; Sture, S. Lunar Surface: Dust Dynamics and Regolith Mechanics. *Rev. Geophys.* **2007**, *45* (2), 1–26.

(13) Caston, R.; Luc, K.; Hendrix, D. Assessing Toxicity and Nuclear and Mitochondrial DNA Damage Caused by Exposure of Mammalian Cells to Lunar Regolith Simulants. *GeoHealth* **2018**, *2*, 139–148.

(14) McKay, D. S.; Blacic, J. D.; Center, N. J. S. LPI Technical Report 91-01. In *Workshop on Production and Uses of Simulated Lunar Materials. A Lunar and Planetary Institute Workshop*; McKay, D. S., Blacic, J. D., Eds.; Lunar and Planetary Institute, 3303 NASA Road 1, Houston, TX 77058: The Lunar and Planetary Institute, in Houston, Texas, 1989; Vol. 1, p 83.

(15) Wentworth, S. J.; Keller, L. P.; McKay, D. S.; Morris, R. V. Space Weathering on the Moon: Patina on Apollo 17 Samples 75075 and 76015. *Meteorit. Planet. Sci.* **1999**, *34* (4), 593–603.

(16) Liu, Y.; Taylor, L. A.; Thompson, J. R.; Schnare, D. W.; Park, J.-S. S. Unique Properties of Lunar Impact Glass: Nanophase Metallic Fe Synthesis. *Am. Mineral.* **2007**, *92* (8–9), 1420–1427.

(17) James, C. L.; Letsinger, S. L.; Basu, A.; Wentworth, S. J.; McKay, D. S. Size

Distribution of Fe0 Globules in Lunar Agglutinitic Glass. *33rd Annu. Lunar Planet. Sci. Conf.* **2002**.

(18) Wallace, W. T.; Phillips, C. J.; Jeevarajan, A. S.; Chen, B.; Taylor, L. A. Nanophase Iron-Enhanced Chemical Reactivity of Ground Lunar Soil. *Earth Planet. Sci. Lett.* **2010**, *295*, 571–577.

(19) Fubini, B.; Hubbard, A. Reactive Oxygen Species (ROS) and Reactive Nitrogen Species (RNS) Generation by Silica in Inflammation and Fibrosis. *Free Radic. Biol. Med.* **2003**, *34* (12), 1507–1516.

(20) Hurowitz, J. A.; Tosca, N. J.; McLennan, S. M.; Schoonen, M. A. A. Production of Hydrogen Peroxide in Martian and Lunar Soils. *Earth Planet. Sci. Lett.* **2007**, *255* (1–2), 41–52.

(21) Horwell, C. J.; Fenoglio, I.; Fubini, B. Iron-Induced Hydroxyl Radical Generation from Basaltic Volcanic Ash. *Earth Planet. Sci. Lett.* **2007**, *261* (3–4), 662–669.

(22) Witze, A. NASA Seeks Better Fake Space Dirt. *Nature* **2017**, *547*, 146–147.

(23) LEAG-CAPTEM. *Status of Lunar Regolith Simulant and Demand for Apollo Lunar Samples*; Marshall Space Flight Center, Alabama 35812, 2010.

(24) Esposito, S.; Marocco, A; Bonelli, B.; Pansini, M. Produzione Di Materiali Compositi Metallo-Ceramici Nano Strutturati Da Precursori Zeolitici Italian Patent. MI 2014 A 000522, 2014.

(25) Esposito, S.; Marocco, A; Bonelli, B.; Pansini, M. Production of Magnetic Metal Nanoparticles Embedded in a Silica-Alumina Matrix. World Patent. WO 2015/145230 A1, 2015.

(26) Marocco, A.; Dell'Agli, G.; Esposito, S.; Pansini, M. Metal-Ceramic Composite Materials from Zeolite Precursor. *Solid State Sci.* **2012**, *14* (3), 394–400.

(27) Ronchetti, S.; Turcato, E. A.; Delmastro, A.; Esposito, S.; Ferone, C.; Pansini, M.; Onida, B.; Mazza, D. Study of the Thermal Transformations of Co- and Fe-Exchanged Zeolites A and X by "in Situ" XRD under Reducing Atmosphere. *Mater. Res. Bull.* **2010**, *45* (6), 744–750.

(28) Barrera, G.; Tiberto, P.; Esposito, S.; Marocco, A.; Bonelli, B.; Pansini, M.; Manzoli, M.; Allia, P. Magnetic Clustering of Ni2+ Ions in Metal-Ceramic Nanocomposites Obtained from Ni-Exchanged Zeolite Precursors. *Ceram. Int.*

**2018**, *44* (14), 17240–17250.

(29) Esposito, S.; Dell'Agli, G.; Marocco, A.; Bonelli, B.; Allia, P.; Tiberto, P.; Barrera, G.; Manzoli, M.; Arletti, R.; Pansini, M. Magnetic Metal-Ceramic Nanocomposites Obtained from Cation-Exchanged Zeolite by Heat Treatment in Reducing Atmosphere. *Microporous Mesoporous Mater.* **2018**, *268*, 131–143.

(30) Barrera, G.; Tiberto, P.; Allia, P.; Bonelli, B.; Esposito, S.; Marocco, A.; Pansini, M.; Leterrier, Y. Magnetic Properties of Nanocomposites. *Appl. Sci.* **2019**, *9* (2), article number 212.

(31) Pansini, M.; Dell'Agli, G.; Marocco, A.; Netti, P. A.; Battista, E.; Lettera, V.; Vergara, P.; Allia, P.; Bonelli, B.; Tiberto, P.; et al. Preparation and Characterization of Magnetic and Porous Metal-Ceramic Nanocomposites from a Zeolite Precursor and Their Application for DNA Separation. *J. Biomed. Nanotechnol.* **2017**, *13* (3), 337–348.

(32) Pansini, M.; Sannino, F.; Marocco, A.; Allia, P.; Tiberto, P.; Barrera, G.; Polisi, M.; Battista, E.; Netti, P. A.; Esposito, S. Novel Process to Prepare Magnetic Metal-Ceramic Nanocomposites from Zeolite Precursor and Their Use as Adsorbent of Agrochemicals from Water. *J. Environ. Chem. Eng.* **2018**, *6* (1), 527–538.

(33) CLASS- Exolith Lab. Planetary Simulant Database https://sciences.ucf.edu/class/exolithlab/.

(34) Mckay, D. S.; Carter, J. L.; Boles, W. W.; Allen, C. C.; Allton, J. H. Jsc-1: A New Lunar Soil Simulant. *Lunar Planet. Inst., Twenty-Fourth Lunar Planet. Sci. Conf.* **1993**, 963–964.

(35) Taylor, L. A.; Pieters, C. M.; Britt, D. Evaluations of Lunar Regolith Simulants. *Planet. Space Sci.* **2016**, *126*, 1–7.

(36) Roux, V.; Roth, M. Off Planet Research, LLC.

(37) Taylor, P. T.; Lowman, P. D.; Nagihara, S.; Milam, M. B.; Nakamura, Y. Jurassic Diabase from Leesburg, VA: A Proposed Lunar Simulant. In *NLSI Lunar Science Conference, held July 20-23, 2008 at NASA Ames Research Center, Moffett Field, California, LPI Contribution No. 1415, abstract no. 2054.*; 2008.

(38) Stoeser, D. B.; Wilson, S.; Rickman, D. L. *Design and Specifications for the Highland Regolith Prototype Simulants NU-LHT-1M and -2M*; National

Aeronautics and Space Administration, Marshall Space Flight Center: Marshall Space Flight Center, Alabama 35812, 2010.

(39) Battler, M. M.; Spray, J. G. The Shawmere Anorthosite and OB-1 as Lunar Highland Regolith Simulants. *Planet. Space Sci.* **2009**, *57* (14–15), 2128–2131.

(40) Kruzelecky, R. V.; Aïssa, B.; Wong, B.; Haddad, E.; Jamroz, W.; Cloutis, E.; Rosca, I. D.; Hoa, S. V.; Therriault, D.; Ellery, A.; et al. Project Moondust: Characterization and Mitigation of Lunar Dust. In *41st International Conference on Environmental Systems 2011, ICES 2011*; 2011; pp 1–19.

(41) Zheng, Y.; Wang, S.; Ouyang, Z.; Zou, Y.; Liu, J.; Li, C.; Li, X.; Feng, J. CAS-1 Lunar Soil Simulant. *Adv. Sp. Res.* **2009**, *43* (3), 448–454.

(42) Liu, A.; Shi, Z.; Hu, X.; Gao, B.; Wang, Z. Lunar Soil Simulant Electrolysis Using Inert Anode for Al-Si Alloy and Oxygen Production. *J. Electrochem. Soc.* **2017**, *164* (2), H126–H133.

(43) Jiang, M.; Li, L.; Sun, Y. Properties of TJ-1 Lunar Soil Simulant. *J. Aerosp. Eng.* **2011**, *25* (3), 463–469.

(44) Sun, H.; Yi, M.; Shen, Z.; Zhang, X.; Ma, S. Developing a New Controllable Lunar Dust Simulant: BHLD20. *Planet. Space Sci.* **2017**, *141*, 17–24.

(45) Tang, H.; Li, X.; Zhang, S.; Wang, S.; Liu, J.; Li, S.; Li, Y.; Wu, Y. A Lunar Dust Simulant: CLDS-I. *Adv. Sp. Res.* **2017**, *59* (4), 1156–1160.

(46) Li, Y.; Liu, J.; Yue, Z. NAO-1: Lunar Highland Soil Simulant Developed in China. *J. Aerosp. Eng.* **2009**, *22* (1), 53–57.

(47) Sueyoshi, K.; Watanabe, T.; Nakano, Y. Reaction Mechanism of Various Types of Lunar Soil Simulants by Hydrogen Reduction. *Earth Sp. 2008* **2008**, No. 1991, 1–8.

(48) Hiroshi, K.; Satoru, U.; Tetsuji, Y.; Shinji, M.; Kenji, T. Properties of Lunar Soil Simulant Manufactured in Japan. *Sp. 98* **1998**, 462–468.

(49) Matsushima, T.; Katagiri, J. 3D Shape Characterization and Image-Based DEM Simulation of the Lunar Soil Simulant FJS-1. *J. Aerosp. Eng.* **2009**, *22* (1), 15–23.

(50) Cesaretti, G.; Dini, E.; De Kestelier, X.; Colla, V.; Pambaguian, L. Building Components for an Outpost on the Lunar Soil by Means of a Novel 3D Printing Technology. *Acta Astronaut.* **2014**, *93*, 430–450.

(51) Marocco, A.; Pansini, M.; Dell'Agli, G.; Esposito, S. *Parameters Expediting the Thermal Conversion of Ba-Exchanged Zeolite A to Monoclinic Celsian*; 2010; Vol. 2010.

(52) Marocco, A.; Dell'Agli, G.; Esposito, S.; Pansini, M. The Role of Residual Na+ and Li+ on the Thermal Transformation of Ba-Exchanged Zeolite A. *Solid State Sci.* **2011**, *13* (5), 1143–1151.

(53) Weidenthaler, C.; Zibrowius, B.; Schimanke, J.; Mao, Y.; Mienert, B.; Bill, E.; Schmidt, W. Oxidation Behavior of Ferrous Cations during Ion Exchange into Zeolites under Atmospheric Conditions. *Microporous Mesoporous Mater.* **2005**, *84* (1–3), 302–317.

(54) Breck, D. W. *Zeolite Molecular Sieves: Structure, Chemistry, and Use*, Wiley.; Jonh Wiley and Sons, Ed.; 1973.

(55) Dyer, A. *An Introduction to Zeolite Molecular Sieves by Alan Dyer*; Stewart, A., Ed.; Wiley Online Library: Chichester; 1988; Vol. 14.

(56) Dell'Agli, G.; Ferone, C.; Mascolo, G.; Pansini, M. Crystallization of Monoclinic Zirconia from Metastable Phases. *Solid State Ionics* **2000**, *127* (3–4), 223–230.

(57) Esposito, S.; Marocco, A.; Dell'Agli, G.; De Gennaro, B.; Pansini, M. Relationships between the Water Content of Zeolites and Their Cation Population. *Microporous Mesoporous Mater.* **2015**, *202*, 36–43.

(58) Strangway, D. W.; Chapman, W. B.; Olhoeft, G. R.; Carnes, J. G. Electrical Properties of Lunar Soil Dependence on Frequency, Temperature and Moisture. *Earth Planet. Sci. Lett.* **1972**, *16*, 275–281.

(59) Alvarez, R. Lunar Powder Simulator under Lunarlike Conditions - Dielectric Properties. *J. Geophys. Res.* **1973**, *78*, 6833–6844.

(60) Marocco, A.; Dell'Agli, G.; Spiridigliozzi, L.; Esposito, S.; Pansini, M. The Multifarious Aspects of the Thermal Conversion of Ba-Exchanged Zeolite A to Monoclinic Celsian. *Microporous Mesoporous Mater.* **2018**, *256*, 235–250.

(61) Esposito, S.; Dell'Agli, G.; Marocco, A.; Bonelli, B.; Allia, P.; Tiberto, P.; Barrera, G.; Manzoli, M.; Arletti, R.; Pansini, M. Magnetic Metal-Ceramic Nanocomposites Obtained from Cation-Exchanged Zeolite by Heat Treatment in Reducing Atmosphere. *Microporous Mesoporous Mater.* **2018**, *268*, 131–143.

(62) Marocco, A.; Liguori, B.; Dell'Agli, G.; Pansini, M. Sintering Behaviour of Celsian Based Ceramics Obtained from the Thermal Conversion of (Ba, Sr)-Exchanged Zeolite A. *J. Eur. Ceram. Soc.* **2011**, *31* (11), 1965–1973.

(63) Bryan, N.; Lasseuguette, E.; van Dalen, M.; Permogorov, N.; Amieiro, A.; Brandani, S.; Ferrari, M.-C. Development of Mixed Matrix Membranes Containing Zeolites for Post-Combustion Carbon Capture. *Energy Procedia* **2014**, *63*, 160–166.

(64) Charkhi, A.; Kazemian, H.; Kazemeini, M. Optimized Experimental Design for Natural Clinoptilolite Zeolite Ball Milling to Produce Nano Powders. *Powder Technol.* **2010**, *203* (2), 389–396.

(65) Liu, Y. .; Thompson, J. R. .; Taylor, L. ~A. .; Park, J. Magnetic Properties of Unique Apollo 17 Soil 70051. In *37th Annual Lunar and Planetary Science Conference,* ; League City, Texas, 2006.

(66) Nagata, T.; Ishikawa, Y.; Kinoshita, H.; Kono, M.; Syono, Y.; Fisher, R. M. Magnetic Properties and Natural Remanent Magnetization of Lunar Materials. In *Geochimica et Cosmochimica Acta Supplement, Volume 1. Proceedings of the Apollo 11 Lunar Science Conference held 5-8 January*; PERGAMON PRESS, INC.,, NEW YORK, United States: Houston, Tex., 1970; pp 2325–2340.

(67) Pearce, G. W.; Strangway, D. W.; Gose, W. A. Magnetic Properties of Apollo Samples and Implications for Regolith Formation. In *5th Lunar Science Conference; March 18-22, 1974; Houston, TX*; Pergamon Press, Inc.: Houston, Tex., 1974; pp 2815–2826.

(68) Brecher, A.; Menke, W. H.; Morash, K. R. Comparative Magnetic Studies of Some Apollo 17 Rocks and Soils and Their Implications. In *5th Lunar Science Conference; March 18-22, 1974; Houston, TX*; New York, Pergamon Press, Inc., 1974; pp 2795–2814.

(69) Cremers, C. J. Thermal Conductivity of Apollo 12 Fines at Intermediate Density. *moon* **1972**, *4* (1–2), 88–92.

(70) Howard, H. T.; Tyler, G. L. Bistatic-Radar Observations of the Lunar Surface with Apollos 14 and 15. *Abstr. Lunar Planet. Sci. Conf.* **1972**, *3*, 398.

(71) Wagner, K. W. Erklärung Der Dielektrischen Nachwirkungsvorgänge Auf Grund

Maxwellscher Vorstellungen. *Arch. für Elektrotechnik* **1914**, *2* (9), 371–387.

(72) Sillars, R. W. The Properties of a Dielectric Containing Semiconducting Particles of Various Shapes. *Inst. Electr. Eng. - Proc. Wirel. Sect. Inst.* **1937**, *12* (35), 139–155.

(73) Sidebottom, D. L.; Roling, B.; Funke, K. Ionic Conduction in Solids: Comparing Conductivity and Modulus Representations with Regard to Scaling Properties. *Phys. Rev. B* **2000**, *63* (2), 024301.

(74) Jonscher, A. K. The 'Universal' Dielectric Response. *Nature* **1977**, *267*, 673.

(75) Olhoeft, G. R.; Frisillo, A. L.; Strangway, D. W. Electrical Properties of Lunar Soil Sample 15301,38. *J. Geophys. Res.* **1974**, *79* (11), 1599–1604.

(76) Olhoeft, G. R.; Frisillo, A. L.; Strangway, D. W. Electrical Properties of Lunar Soil Sample 15301,38. *J. Geophys. Res.* **1974**, *79* (11), 1599–1604.

(77) *Lunar Sourcebook: A User's Guide to the Moon*; Heiken, G. H. ., Vaniman, D. T. ., French, B. M., Eds.; Press Syndicate of the University of Cambridge: New York, 1991.

(78) Schwerer, F. C.; Huffman, G. P.; Fisher, R. M.; Nagata, T. Electrical Conductivity of Lunar Surface Rocks - Laboratory Measurements and Implications for Lunar Interior Temperatures. In *Lunar Science Conference, 5th, Houston, Tex., March 18-22, 1974*; New York, Pergamon Press, I., Ed.; 1974; pp 2673–2687.

(79) Meyer, C. *14163 Bulk Soil Sample 7,776 Grams*; 2011.

(80) Meyer, C. *15301 Soil 1244.1 Grams*; 2010.

TOC


cation exchange
step 1
reductive thermal treatment
step 2
glassy matrix
np-Fe0
zeolite
CE-zeolite
Simulated Moon Agglutinates

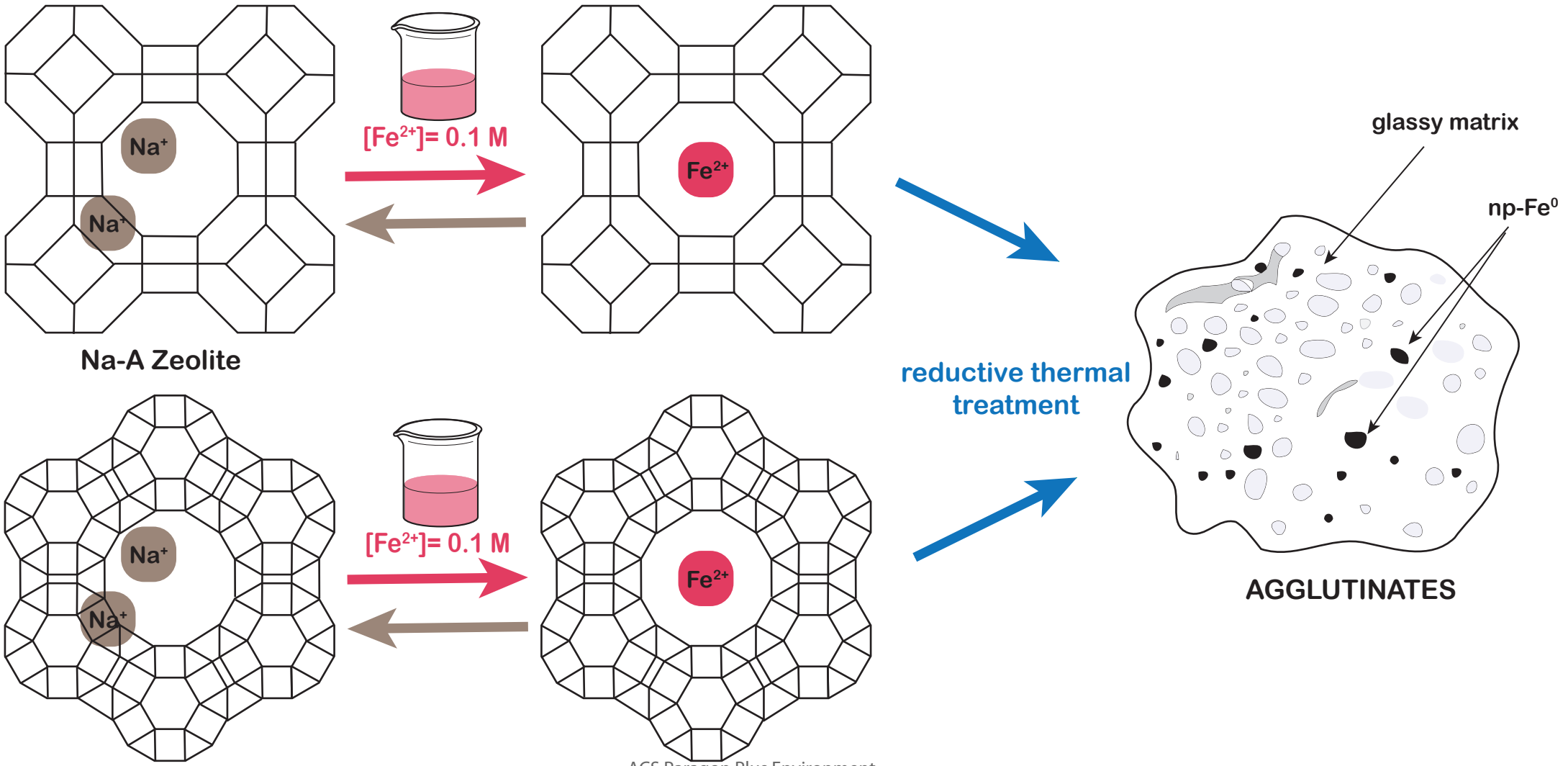
Na+
Na+
[Fe2+]= 0.1 M
Fe2+
Na-A Zeolite
Na+
Na+
[Fe2+]= 0.1 M
Fe2+
Na-X Zeolite
reductive thermal treatment
glassy matrix
np-Fe0
AGGLUTINATES

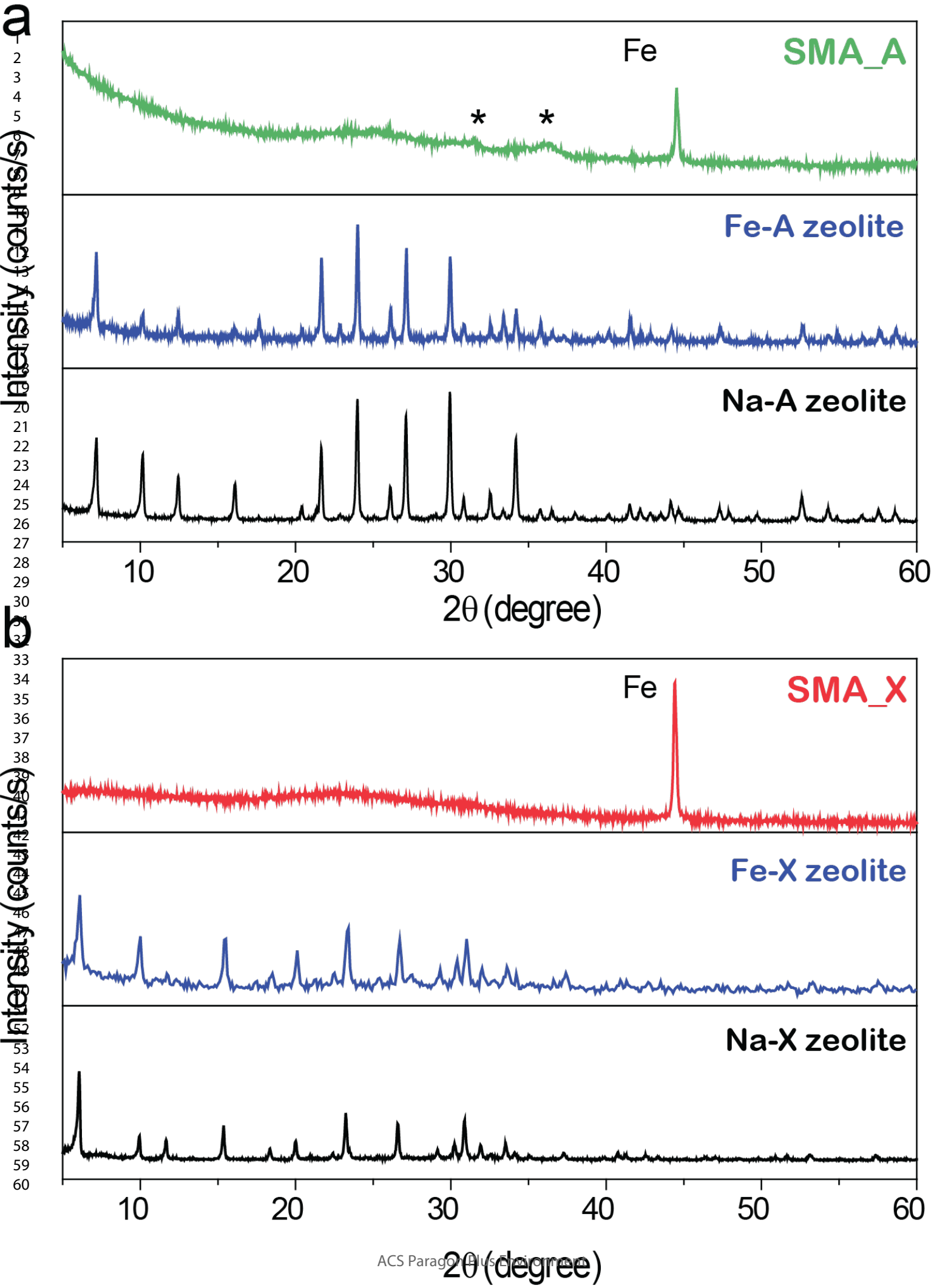
a
Fe
SMA_A
*
*
Fe-A zeolite
Na-A zeolite
Intensity (counts/s)
10
20
30
40
50
60
2θ (degree)
c
Fe
SMA_X
Fe-X zeolite
Na-X zeolite
Intensity (counts/s)
10
20
30
40
50
60
2θ (degree)

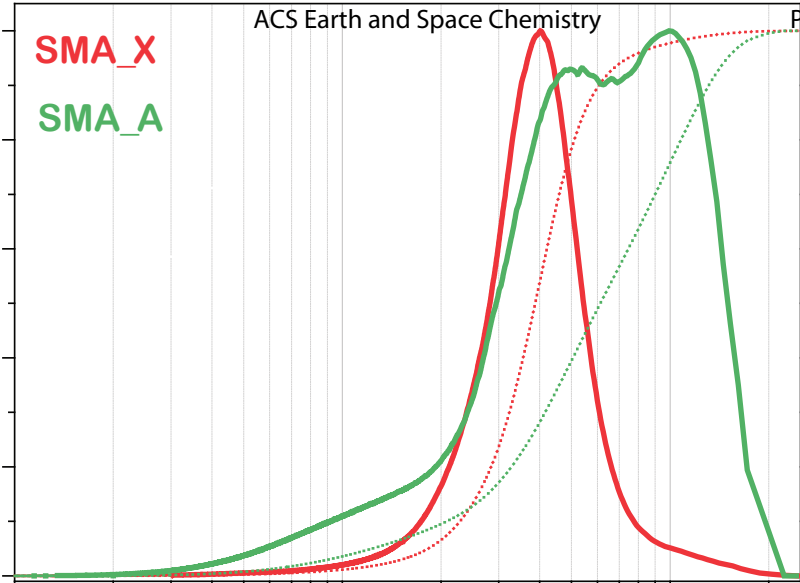
SMA_X
SMA_A
Relative weight
Cumulative (%)
Diameter (μm)
0.0
0.2
0.4
0.6
0.8
1.0
0
20
40
60
80
100
0.1
1
10

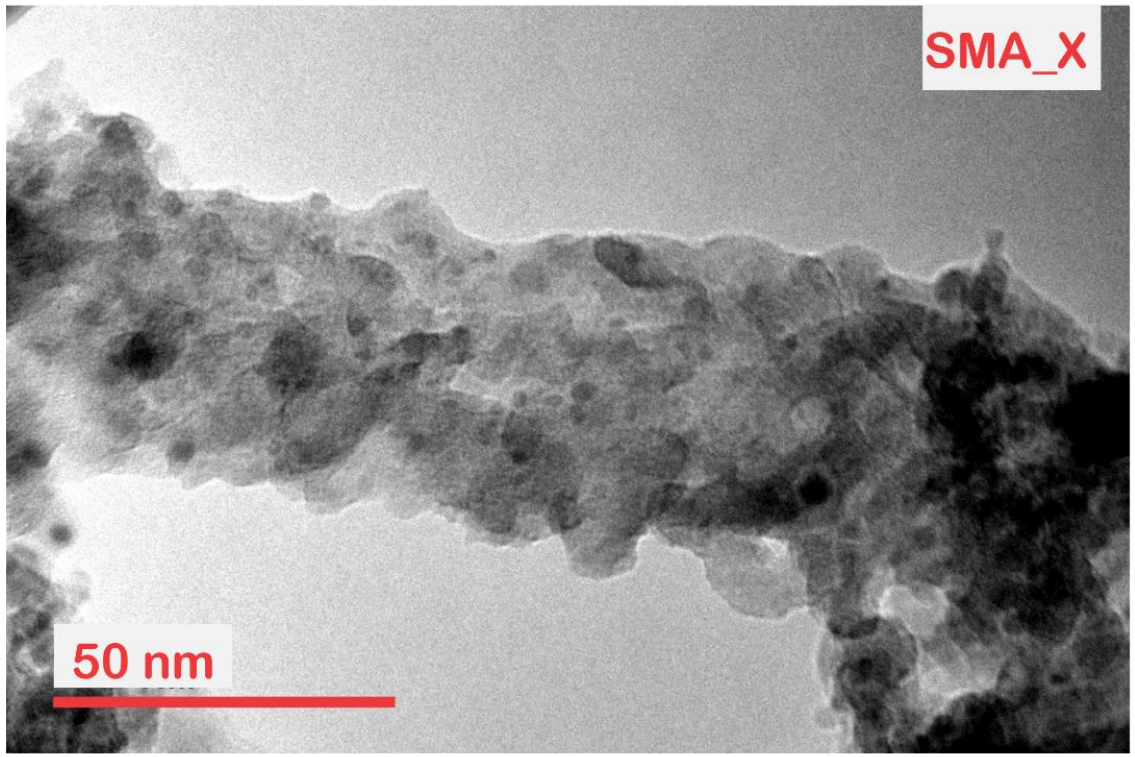
SMA_X
50 nm

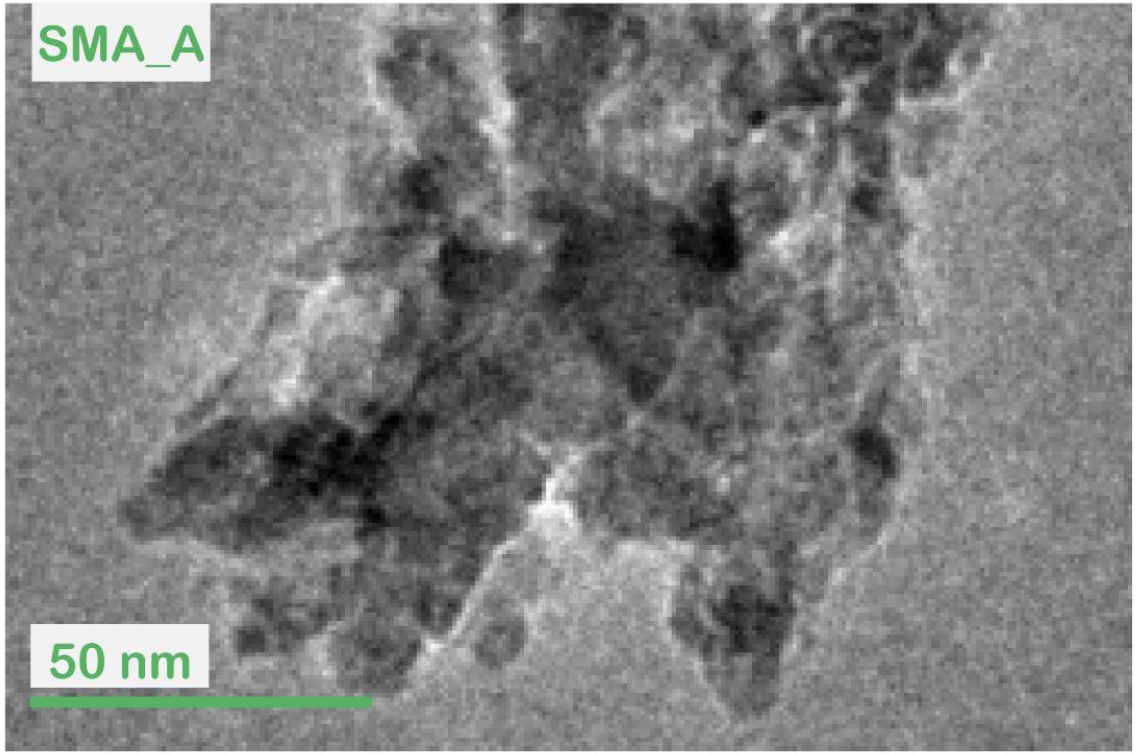
SMA_A
50 nm

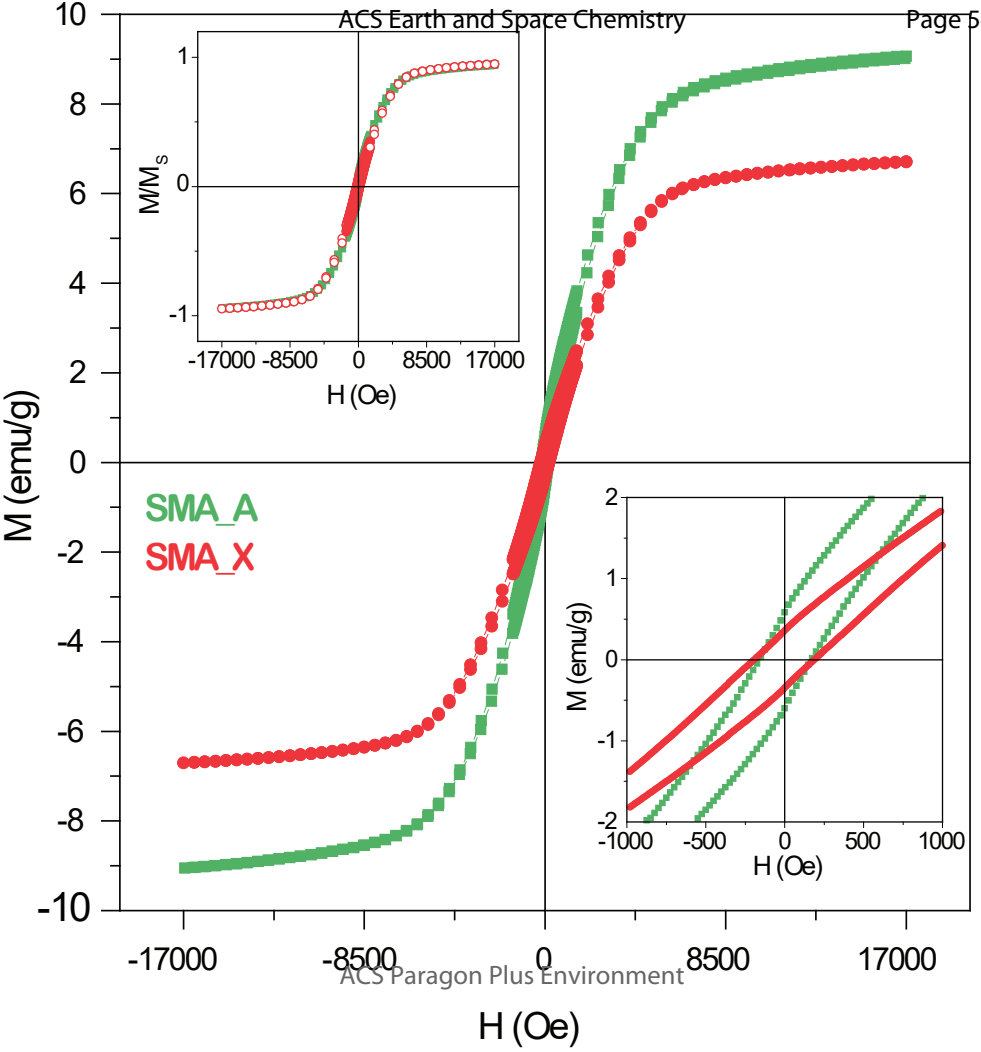

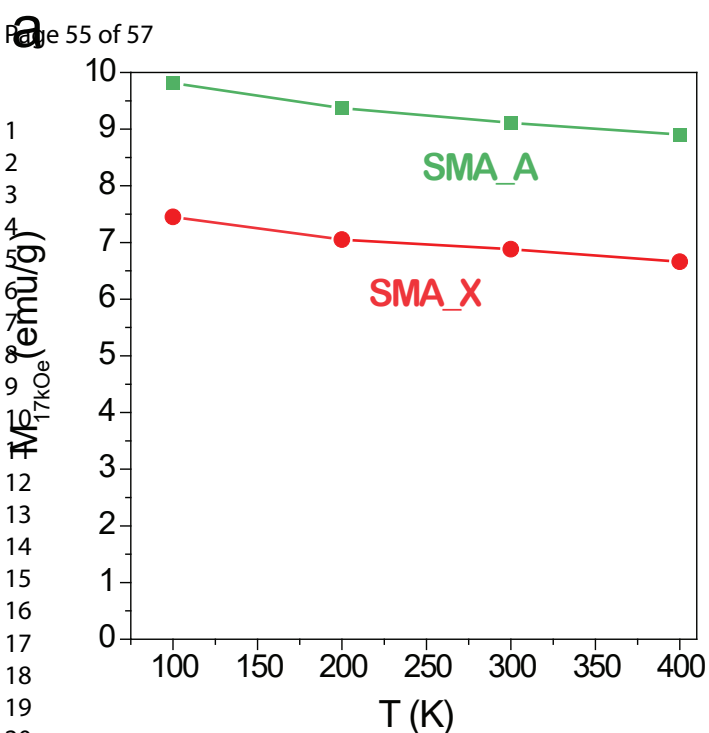


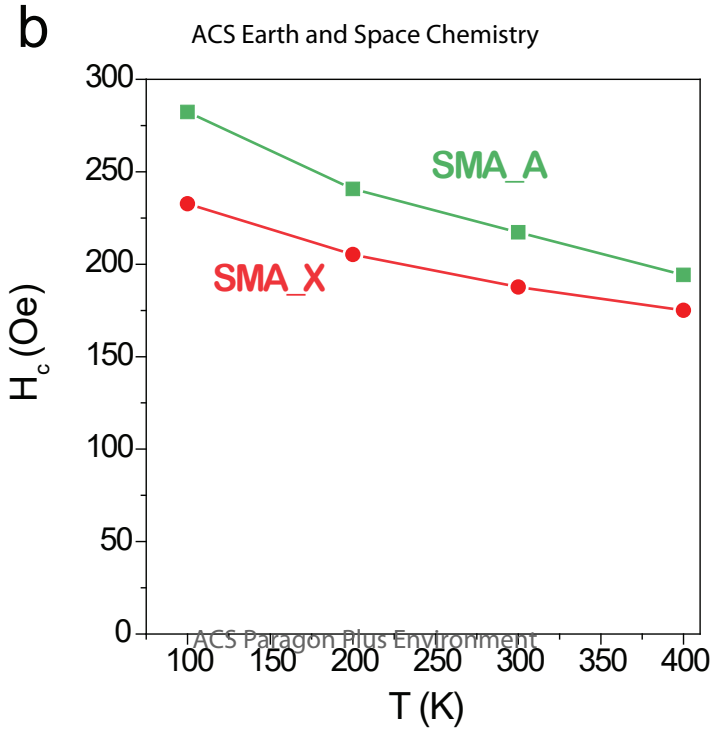


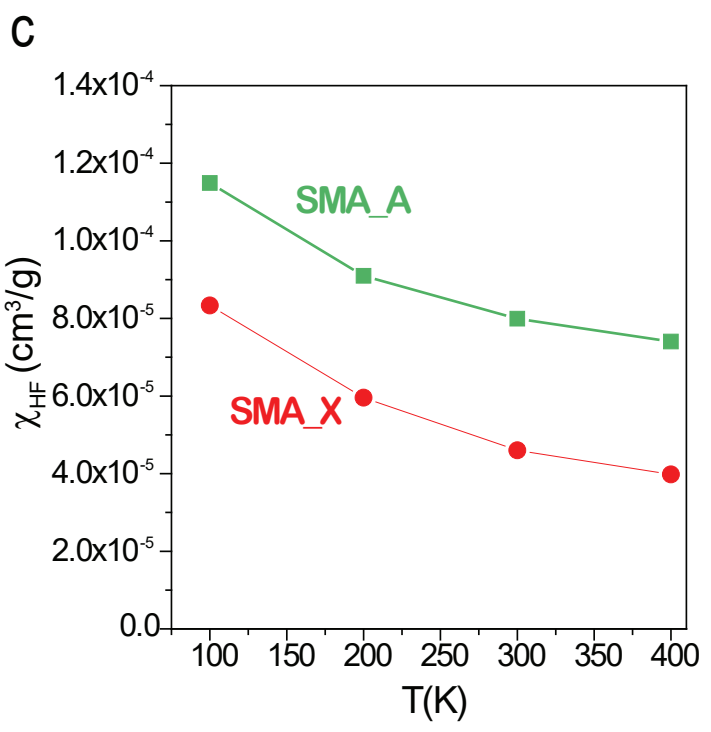

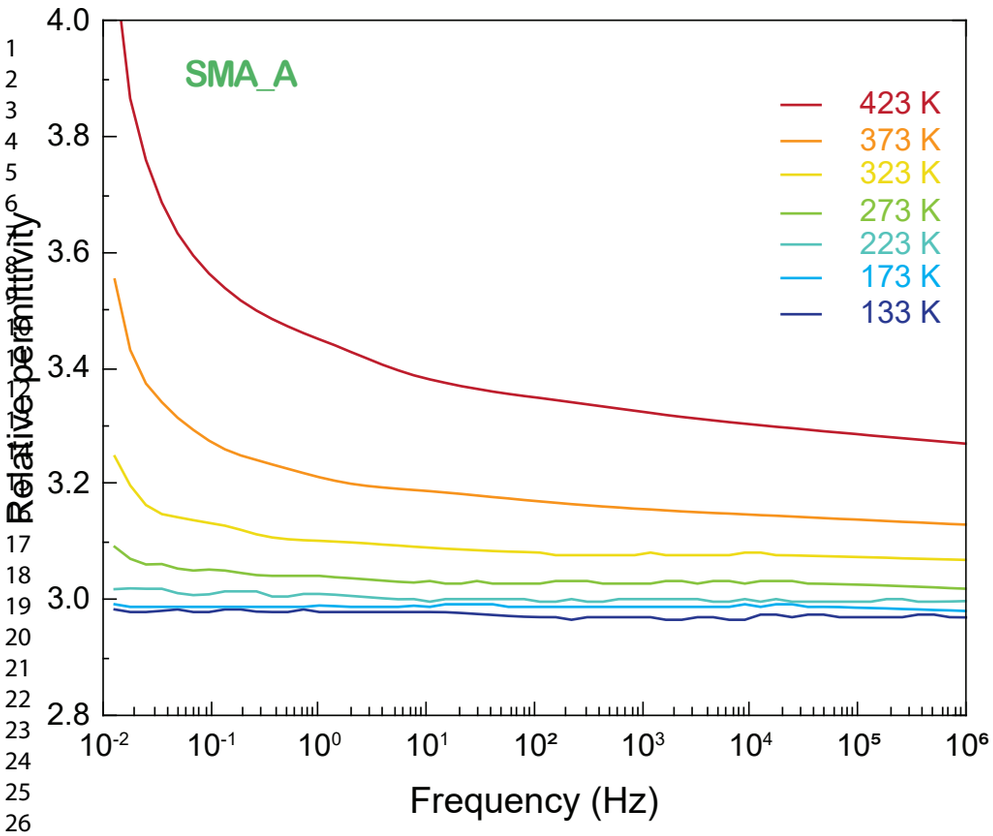
a
SMA_A
423 K
373 K
323 K
273 K
223 K
173 K
133 K
Relative permittivity
Frequency (Hz)

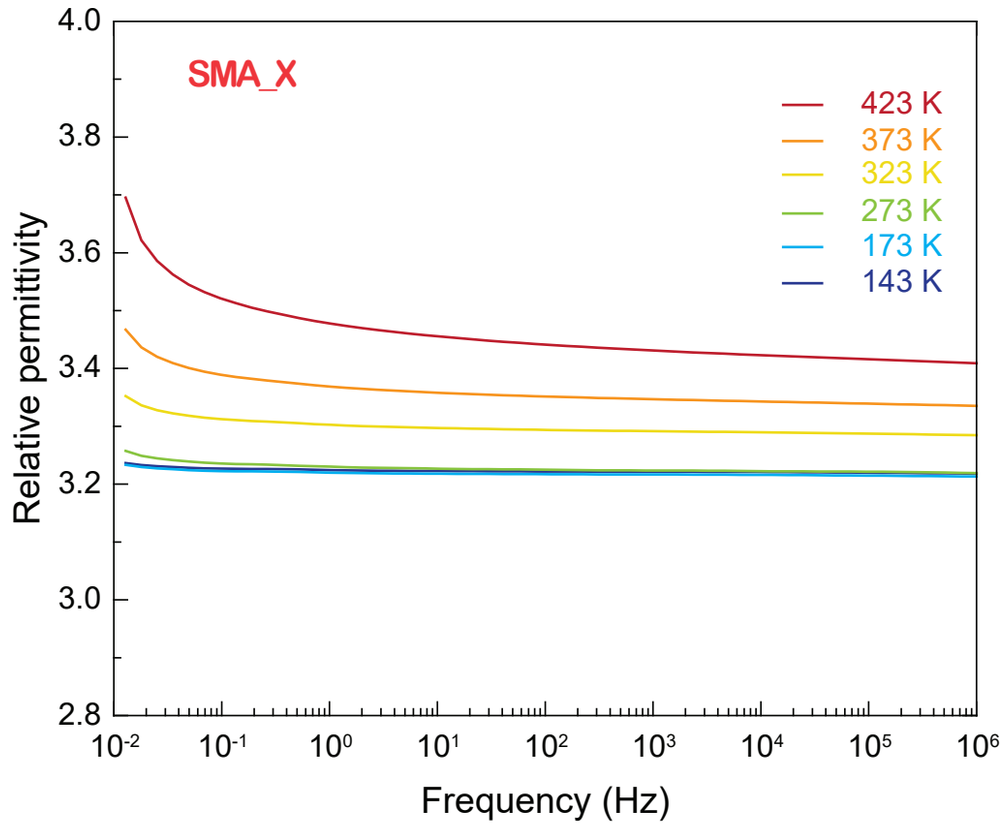
b
SMA_X
423 K
373 K
323 K
273 K
173 K
143 K
Relative permittivity
Frequency (Hz)

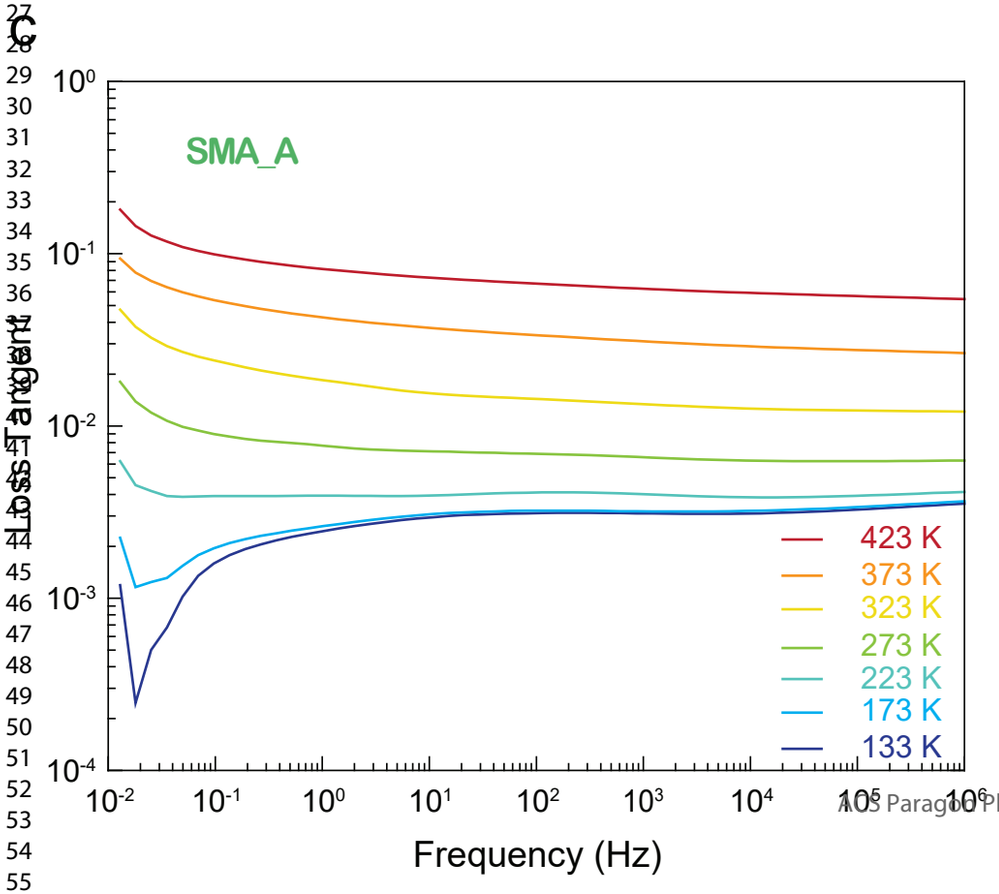
c
SMA_A
423 K
373 K
323 K
273 K
223 K
173 K
133 K
Loss Tangent
Frequency (Hz)

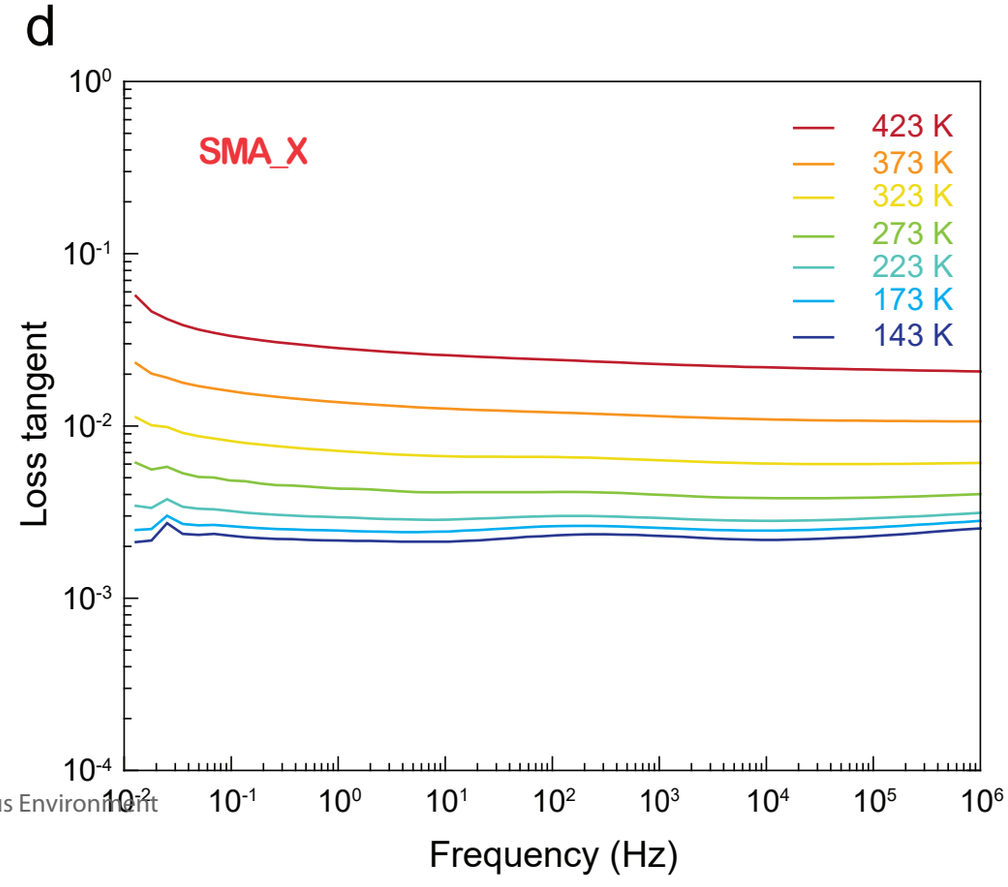
d
SMA_X
423 K
373 K
323 K
273 K
223 K
173 K
143 K
Loss tangent
Frequency (Hz)

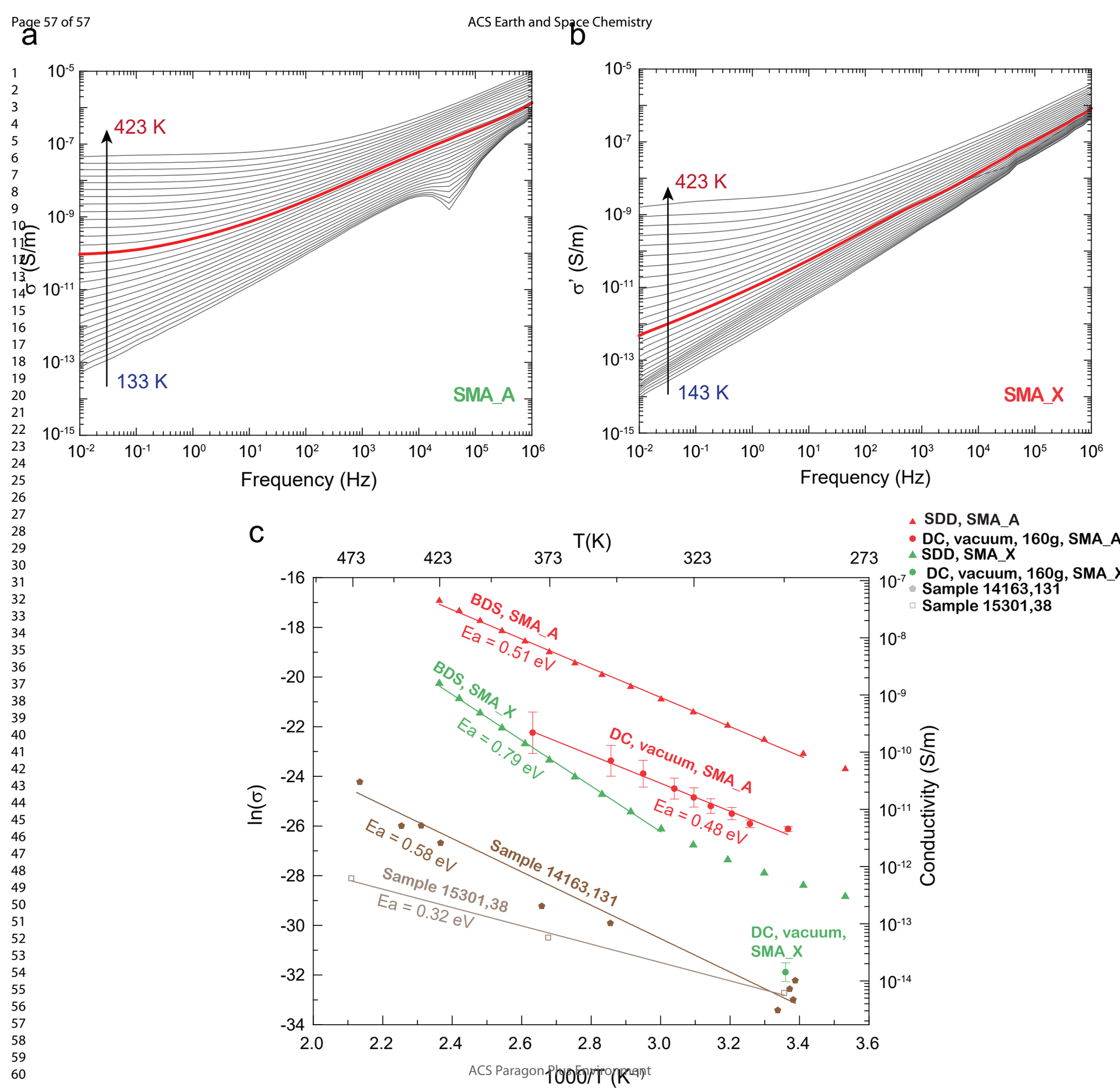
a
423 K
133 K
SMA_A
σ' (S/m)
Frequency (Hz)
b
423 K
143 K
SMA_X
σ' (S/m)
Frequency (Hz)
c
T(K)
473
423
373
323
273
SDD, SMA_A
DC, vacuum, 160g, SMA_A
SDD, SMA_X
DC, vacuum, 160g, SMA_X
Sample 14163,131
Sample 15301,38
BDS, SMA_A
Ea = 0.51 eV
BDS, SMA_X
Ea = 0.79 eV
DC, vacuum, SMA_A
Ea = 0.48 eV
Ea = 0.58 eV
Sample 14163,131
Sample 15301,38
Ea = 0.32 eV
DC, vacuum, SMA_X
ln(σ)
Conductivity (S/m)
1000/T (K⁻¹)